2011

# Hydrodesulfurization and hydrodeoxygenation over noble metal phosphide catalysts

Richard H. Bowker
*Western Washington University*

# HYDRODESULFURIZATION AND HYDRODEOXYGENATION OVER NOBLE METAL PHOSPHIDE CATALYSTS

By

Richard H. Bowker

Accepted in Partial Completion

Of the Requirements for the Degree

Master of Science

---

Moheb A. Ghali, Dean of the Graduate School

ADVISORY COMMITTEE

---

Chair, Dr. Mark E. Bussell

---

Dr. John D. Gilbertson

---

Dr. Gregory W. O'Neil

**MASTER'S THESIS**

In presenting this thesis in partial fulfillment of the requirements for a master's degree at Western Washington University, I grant to Western Washington University the non-exclusive royalty-free right to archive, reproduce, distribute, and display the thesis in any and all forms, including electronic format, via any digital library mechanisms maintained by WWU.

I represent and warrant this is my original work, and does not infringe or violate any rights of others. I warrant that I have obtained written permissions from the owner of any third party copyrighted material included in these files.

I acknowledge that I retain ownership rights to the copyright of this work, including but not limited to the right to use all or part of this work in future works, such as articles or books.

Library users are granted permission for individual, research and non-commercial reproduction of this work for educational purposes only. Any further digital posting of this document requires specific permission from the author.

Any copying or publication of this thesis for commercial purposes, or for financial gain, is not allowed without my written permission.

Richard H. Bowker

November 1, 2011

# HYDRODESULFURIZATION AND HYDRODEOXYGENATION OVER NOBLE METAL PHOSPHIDE CATALYSTS

A Thesis

Presented to

The Faculty of

Western Washington University

In Partial Fulfillment

Of the Requirements for the Degree

Master of Science

by

Richard H. Bowker

November 2011

## Abstract

As the demand and price for crude petroleum continues to increase, unconventional sources of petroleum, including tar sands, oil shales, and bio-derived oils have become economically viable feedstocks. Previously, these oil reserves were deemed too costly to process into fuels due to the high impurity content (S, N, O) of the unrefined feedstocks. The decline in conventional oil reserves has focused increasing attention on utilizing these unconventional feedstocks. However, stringent environmental regulations governing fuel impurity content require refineries to remove these impurities in increasing amounts. Current hydrotreatment catalysts are unable to effectively remove theses impurities in sufficient quantities to meet government regulation. The goal of this research is to develop more effective hydrotreatment catalysts for upgrading unconventional feedstocks and producing ultra clean fuels.

Previous research in the Bussell laboratory has shown that silica-supported nickel phosphide ($Ni_2P/SiO_2$) catalysts were highly effective at processing high boiling-point, organosulfur impurities and had excellent resistance to sulfur deactivation. In this research, several silica-supported noble metal phosphide catalysts were prepared and their hydrodesulfurization (HDS) and hydrodeoxygenation (HDO) properties were evaluated and compared with several commercial catalysts. Silica-supported rhodium phosphide ($Rh_2P/SiO_2$) had a higher dibenzothiophene (DBT) HDS activity than either silica-supported rhodium metal ($Rh/SiO_2$) or rhodium sulfide (sulf. $Rh/SiO_2$), and was also more active than a Ni-Mo/$Al_2O_3$ commercial catalyst. Due to limited active site densities in the as-prepared catalysts, silica-supported palladium phosphide ($Pd_3P/SiO_2$, $Pd_5P_2/SiO_2$) catalysts were less

active than the commercial Ni-Mo/$Al_2O_3$ catalyst. However, turnover frequencies (TOFs) and sulfur analyses of the HDS-tested palladium phosphides revealed high DBT HDS activity on a per site basis, and an increased resistance to sulfur incorporation compared to Pd/$SiO_2$, suggesting a high HDS potential for the palladium phosphide catalysts if the site density can be optimized. Silica-supported ruthenium phosphides (RuP/$SiO_2$ and $Ru_2P$/$SiO_2$) were also prepared and tested for furan HDO activity. $Ru_2P$/$SiO_2$ outperformed silica-supported ruthenium (Rh/$SiO_2$) and RuP/$SiO_2$ catalysts, as well as a Co-Mo/$Al_2O_3$ commercial catalyst, while exhibiting excellent selectivity toward $C_4$ hydrocarbon products.

## Acknowledgements

**Research Advisor:**

Dr. Mark E. Bussell

**Thesis Committee Members:**

Dr. John D. Gilbertson
Dr. Gregory W. O'Neil

**Research Group Members:**

John Hayes, Mica Smith, Cameron Moak, Bo Carrillo, Kyle Mikkelsen, Michael Takemura, Amy Gaudette

**Scientific Technical Services:**

Jim Mullen, Geoff Landis, and Clint Burgress

**Advanced Materials Science and Engineering Center:**

Dr. Polly Berseth

**Environmental Molecular Science Laboratory Scientists at Pacific Northwest National Laboratory:**

Dr. Mark Engelhard
Dr. Libor Kovarik
Shail Sanghavi

**Western Washington University Chemistry Department**

**Financial Support** :

National Science Foundation
Ross Travel Grant

## Table of Contents

**Page**

## LIST OF FIGURES

## LIST OF TABLES

**Page**

# Chapter 1. Introduction

## 1.1 Hydrotreatment

Hydrotreating, also referred to as hydroprocessing, encompasses a variety of refinery upgrading processes which utilize hydrogen in the presence of a catalyst to either hydrogenate unsaturated hydrocarbons remaining in crude oil distillate fractions, or to selectively remove heteroatom contaminants, such as sulfur, nitrogen, and oxygen naturally present in crude oil. These two hydrotreatment processes represent several of the most common fuel upgrading processes and, therefore, unsurprisingly account for almost 10% of the worldwide catalyst market.[1]

*Hydrogenation*

Unrefined crude oil consists of a complex mixture of hydrocarbons that can be divided into three major classes: paraffins, naphthenes, and aromatics (Figure 1.1).[2]

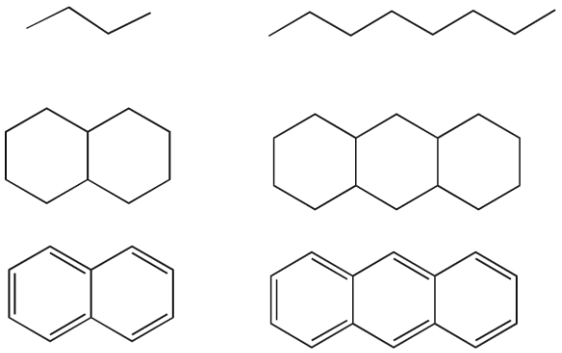

**Figure 1.1 Examples of several compounds found in crude oil, from top to bottom: paraffins, naphthenes, and aromatics.[2]**

With the exception of the lowest boiling point fraction which contains only paraffins, the three types of hydrocarbons are present in varying ratios in all distillate streams. Of these three, aromatic compounds are considered to be the least desirable in distillate streams for several reasons. First, some aromatic compounds are carcinogenic, and, therefore, concentrations are limited in many petroleum products. Second, aromatics tend to have slightly different physical characteristics than the saturated hydrocarbons present in the same distillate fraction, and are considered undesirable in streams destined for fuel use.[1] A good example is diesel fuel, where a high aromatic content results in a delayed ignition point and loss of overall engine efficiency. While highly susceptible to sulfur and nitrogen poisoning, current hydrogenation catalysts are highly effective once the impurities are removed from the distillate stream and are not further considered in this research.

*Feedstock Contamination*

All crude oil contains some form of heteroatom contamination. The type and concentration of the impurities vary greatly depending on the source of the petroleum, but they consist primarily of organosulfur, nitrogen, and oxygen containing hydrocarbons.[1] These impurities are removed through hydrotreatment processes named after the target heteroatom: hydrodesulfurization (HDS), hydrodenitrogenation (HDN), hydrodeoxygenation (HDO), and are accomplished with either a cobalt or nickel promoted molybdenum sulfide catalyst supported on alumina (e.g. Ni-Mo/$Al_2O_3$).[3-4] The heteroatom contaminants must be removed before the distillate fraction is further upgraded because they poison the hydrocracking (HCR), catalytic reforming, and fluid catalytic cracking (FCC) catalysts used in

subsequent downstream refining processes.[2] Additionally, several of these heteroatom impurities, sulfur and nitrogen in particular, when burned in fuels produce emissions known to be environmentally harmful.[5,6] The combustion of organosulfur compounds results in sulfur dioxide ($SO_2$), a precursor to acid rain, while the combustion of organonitrogen compounds results in the formation of nitrogen oxides (NO and $NO_2$), a major component of smog.[7] Because of these deleterious effects, most governments place severe restrictions that limit the amount of these impurities in final fuel products. While hydrotreating processes and catalysts have been extensively studied and optimized for almost 100 years, changes in both feedstock composition and environmental regulation continue to challenge current catalyst technology.[8]

## 1.2 Changes in Feedstock composition

*Petroleum*

As known oil reserves become exhausted and demand for transportation fuels continues to increase, refineries have been forced to utilize lower quality, unconventional petroleum sources that were previously deemed uneconomical, resulting in a heavier and sourer (higher wt% S content) feedstock composition. As shown in Table 1.1, crude oil can have a wide range of elemental contamination depending on source location.

| | Arabian Light | Arabian Heavy | Attaka (Indonesia) | Boscan | Shale oil | Tar sand | Coal liquid |
|---|---|---|---|---|---|---|---|
| Specific gravity (g $cm^{-3}$) | 0.86 | 0.89 | 0.81 | 0.998 | -- | -- | -- |
| Sulfur (wt%) | 1.8 | 2.9 | 0.07 | 5.2 | 0.7 | 5 | 0.3 |
| Nitrogen (wt%) | 0.1 | 0.2 | <0.1 | 0.7 | 1.6 | 0.5 | 0.9 |
| Oxygen (wt%) | <0.1 | | <0.1 | <0.1 | 1.5 | 0.5 | 3.8 |
| V (ppm) | 18 | 50 | <1 | 1200 | -- | 150 | -- |
| Ni (ppm) | 4 | 16 | <1 | 150 | -- | 75 | -- |

**Table 1.1 Properties of crude oil from various sources.**[1]

For example, a barrel of crude oil obtained from either the Athabasca tar sands or Venezuela contains almost 3 times the amount of sulfur and as much as 15 times as much nitrogen when compared to a barrel of Arabian Light Crude. Additionally, as show in Figure 1.2, crude oil from the Athabasca tar sands in Canada continues to become a larger portion of the total U.S. oil imports, while crude imports from Saudi Arabia continue to decrease.[9] Therefore, because of the increased use of heavier crude feedstocks, refineries have more sulfur and nitrogen to remove, on a weight percent basis, to produce a fuel of a similar or higher quality than they previously produced when oil reserves were yielding higher quality, sweeter crude.

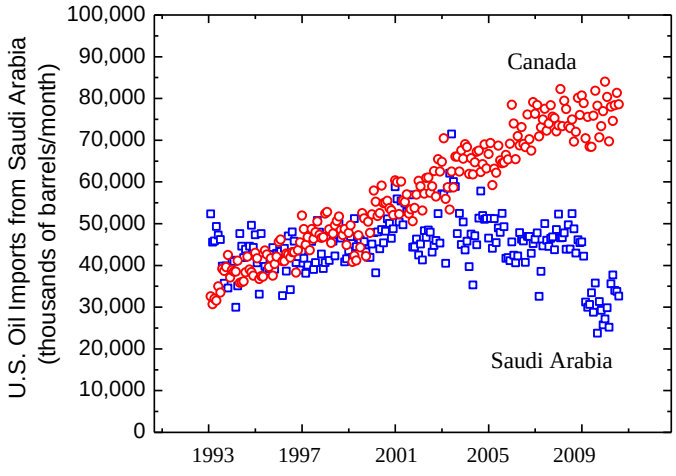


**Figure 1.2 Table of US oil imports from Canada (circles) and Saudi Arabia (squares).**[9]

*Bio-Oils*

In addition to the utilization of unconventional fossil fuel sources like tar sands and shale oils, feedstocks derived from renewable sources, such as bio-oil, are also becoming of interest for several reasons.[10] First, fossil fuel resources are limited and dwindling, and as demand for liquid transportation fuels increases, the development of an economical and sustainable replacement fuel has become imperative. Second, while other renewable energy technologies require substantial infrastructure and processing developments before they can be considered petroleum replacements, bio-oils can be upgraded with conventional hydroprocessing technologies with little change in existing infrastructure and utilized as a drop-in petroleum replacement because the refined product is chemically indistinguishable from petroleum derived fuels.[11]

Similar to unprocessed crude oils, bio-oils consist of a complex mixture of hydrocarbons, with varying amounts of heteroatom contamination.[12] However, unlike most fossil fuel resources, bio-oils contain significant amounts of oxygen because they are derived directly from plant cellulose, hemicellulose, and lignin. Recent research has estimated bio-oils can contain over 300 different oxygen containing compounds, usually in the form of carboxylic acids, alcohols, ethers, aldehydes, esters, ketones, sugars, and furans.[10] This high oxygen content in the bio-oil results in undesirable fuel properties, including low energy density, high viscosity and acidity.[13] Therefore, upgrading the bio-oil by lowering the oxygen content is required before bio-oils can be used as a drop-in replacement for traditional petroleum fuels.

Conventional hydroprocessing catalysts are optimized to remove sulfur and nitrogen from crude oil feedstocks and only process oxygen in small amounts, whereas oxygen represents the major impurity component of bio-oils. Furthermore, these catalysts require the presence of sulfur, usually in the form of $H_2S$ produced during the HDS of a feedstock, to remain catalytically active.[1-2] Bio-oils contain only trace amounts of organosulfur impurities and not enough to produce sufficient amounts of $H_2S$ necessary to maintain catalyst stability. Therefore, either $H_2S$ would need to be co-fed during the hydrotreatment process or new catalysts optimized to remove oxygen without being sulfided need to be developed specifically for bio-oil hydrotreatment.

## 1.3 Environmental Regulation

In an attempt to reduce the negative environmental impacts from burning petroleum-based fuels, governments around the world have continued to decrease the allowable contaminant concentrations in transportation fuels. Conventional industrial HDS catalysts, while effective at removing sulfur from low boiling point organosulfur compounds, are less effective at processing higher boiling point, aromatic organosulfur compounds (Figure 1.3).[1]

**a)** **b)**

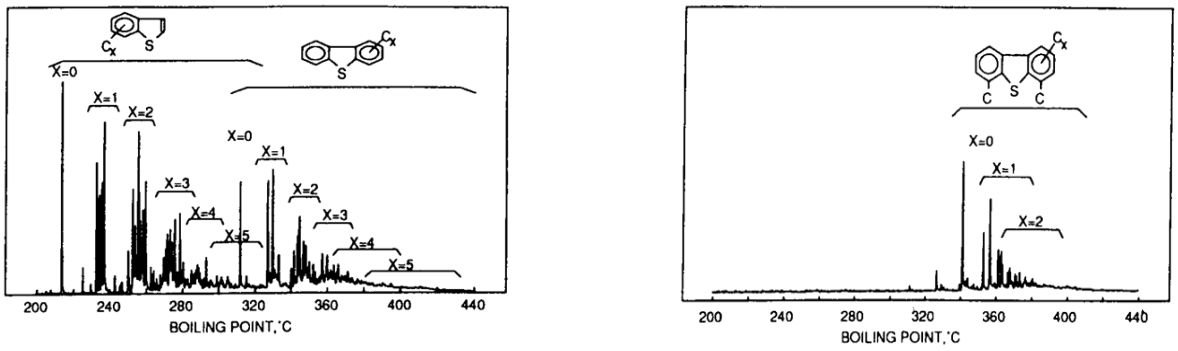


**Figure 1.3 GC traces of light cycle oil prior (a) and after (b) HDS treatment using a traditional industrial catalyst.**[1]

However, as restrictions governing impurity content continue to become more stringent, removal of these high boil point organosulfur compounds, through a process termed deep HDS, has become essential to achieve these strict environmental regulations.[6]

Several strategies are being investigated to effectively desulfurize the benzothiophene and dibenzothiophene compounds that remain after conventional HDS to produce ultra clean fuels. Some methods propose using conventional catalysts, and achieve ultra clean standards by increasing the size of the catalyst bed, and the temperature and $H_2$ pressure of the HDS reactor. However, this approach is considered economically unsustainable because of the increased operational costs. Other methods propose changes to HDS reactor design and the development of new catalyst technologies to produce ultra clean fuels. One such reactor design, referred to as a sequential or two-stage HDS reactor, is a good example of the combined development of new reactor design and improved catalyst technology.[14] A typical two-stage reactor schematic is shown in figure 1.4.

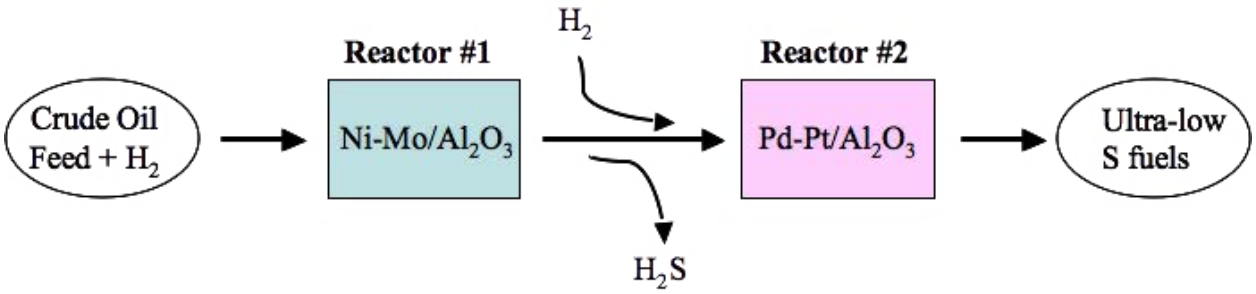


**Figure 1.4 Schematic of a two-stage HDS reactor.**

The first reactor is similar to a typical industrial HDS reactor, and utilizes an alumina supported cobalt or nickel promoted molybdenum sulfide catalyst. Following initial processing, the stream exits the first reactor, where the $H_2S$ produced during HDS is removed from the stream and/or diluted with additional hydrogen. This step is crucial because the noble metal catalysts used in the second reactor, while effective at removing the higher boiling point contaminants in trace amounts, are susceptible to sulfur poisoning under high $H_2S$ pressures.[15-16] Development of more sulfur tolerant and efficient noble metal-based catalysts suitable for use in these two-stage, deep HDS reactors is one of the goals of this research.

## 1.4 Thesis Research Goals

The goal of this thesis research is to synthesize and characterize silica supported noble metal phosphide catalysts using rhodium, palladium, and ruthenium to better understand the experimental conditions necessary to obtain different metal phosphide phases, e.g., RuP vs $Ru_2P$, and to gauge their effect on catalyst particle size. Once successfully synthesized, the dibenzothiophene (DBT) HDS and furan HDO properties of these catalysts will be evaluated and compared with those of silica-supported reduced metal and sulfided metal catalysts in order to determine their potential as hydrotreating catalysts for upgrading petroleum and bio-derived fuel feedstocks.

**References:**


1. Topsøe, H.; Clausen, B. S.; Massoth, F. E., *Hydrotreating catalysis*. Springer: Berlin ; New York, 1996; p ix, 310 p.

2. Gary, J. H.; Handwerk, G. E., *Petroleum refining : technology and economics*. 2nd ed.; M. Dekker: New York, 1984; p ix, 414 p.

3. Bej, S. K.; Maity, S. K.; Turaga, U. T., Search for an efficient 4,6-DMDBT hydrodesulfurization catalyst: A review of recent studies. *Energ. Fuel* **2004,** *18* (5), 1227-1237.

4. Oyama, S. T.; Gott, T.; Zhao, H. Y.; Lee, Y. K., Transition metal phosphide hydroprocessing catalysts: A review. *Catal. Today* **2009,** *143* (1-2), 94-107.

5. Song, C., New Approaches to Deep Desulfurization for Ultra-Clean Gasoline, and Diesel Fuel: An Overview. *Fuel Chemistry Division Preprints* **2002,** *47* (2), 438-444.

6. Pawelec, B.; Navarro, R. M.; Campos-Martin, J. M.; Fierro, J. L. G., Towards near zero-sulfur liquid fuels: a perspective review. *Catal. Sci. Technol.* **2011,** *1* (1), 23-42.

7. Stirling, D., *The sulfur problem: cleaning up industrial feedstocks.* Royal Society of Chemistry: Cambridge, UK, 2000.

8. Satterfield, C. N., *Heterogeneous catalysis in practice*. McGraw-Hill: New York, 1980; p xvi, 416 p.

9. US Energy Information Administration. http://www.eia.gov/dnav/pet/hist/LeafHandler.ashx?n=PET&s=MTTIMUSCA1&f=M (accessed Oct. 2010).

10. Corma, A.; Huber, G. W.; Iborra, S., Synthesis of transportation fuels from biomass: Chemistry, catalysts, and engineering. *Chem. Rev.* **2006,** *106* (9), 4044-4098.

11. Donnis, B.; Egeberg, R. G.; Blom, P.; Knudsen, K. G., Hydroprocessing of Bio-Oils and Oxygenates to Hydrocarbons. Understanding the Reaction Routes. *Top. Catal.* **2009,** *52* (3), 229-240.

12. Zhang, Q.; Chang, J.; Wang, T. J.; Xu, Y., Review of biomass pyrolysis oil properties and upgrading research. *Energ. Convers. Manage.* **2007,** *48* (1), 87-92.

13. Elliott, D. C., Historical developments in hydroprocessing bio-oils. *Energ. Fuel* **2007,** *21* (3), 1792-1815.

14. Stork, W. H. J., Molecules, catalysts and reactors in hydroprocessing of oil fractions. *Hydrotreatment and Hydrocracking of Oil Fractions* **1997,** *106*, 41-67.

15. Centeno, A.; Perez-Martinez, D.; Giraldo, S. A., Effects of the H2S partial pressure on the performance of bimetallic noble-metal molybdenum catalysts in simultaneous hydrogenation and hydrodesulfurization reactions. *Appl. Catal. A-Gen.* **2006,** *315*, 35-43.

16. Arias, P. L.; Barrio, V. L.; Cambra, J. F.; Guemez, M. B.; Pawelec, B.; Fierro, J. L. G., Hydrodesulfurization and hydrogenation of model compounds on silica-alumina supported bimetallic systems. *Fuel* **2003,** *82* (5), 501-509.

# Chapter 2. Experimental Methods

## 2.1 Catalyst Synthesis

Precursors of silica supported rhodium, ruthenium, and palladium metal catalysts were synthesized by impregnating silica ($SiO_2$) with aqueous solutions containing salts of the noble metals. The solution was added dropwise to the silica support until uniform incipient wetness was achieved and the impregnated support was then evaporated to dryness at 382 K. Multiple impregnations were necessary to transfer all the solution onto the support. Several aliquots of nanopure water were used to rinse the beaker originally containing the aqueous metal salt, and these rinses were transferred to the support as described above. The impregnated support was dried for an additional 24 h once all the solution was transferred. The dried catalyst precursor was transferred to a sample vial and labeled appropriately.

All reagents were used as delivered except the silica ($SiO_2$, Cabot, M-7D, 200 $m^2/g$, 99.9%+), which was calcined in air prior to use by heating from room temperature to 773 K at 40 K $min^{-1}$, and holding at that temperature for an additional 3 h. The calcined silica was then stored in an oven at 382 K. All gases were purified with 5 Å molecular sieve (Alltech) and oxygen purification (Oxyclear) traps.

### 2.1.1 Rhodium Catalysts

*Supported rhodium metal ($Rh/SiO_2$)*

A precursor of a silica-supported rhodium metal catalyst ($Rh/SiO_2$) with an Rh loading equivalent to that of a 5 wt% $Rh_2P/SiO_2$ (4.4 wt% Rh) was prepared by dissolving 0.5054 g of rhodium (III) nitrate hydrate ($Rh(NO_3)_3 \bullet H_2O$, Sigma Aldrich, Rh ≅ 36 wt%) in 5

mL nanopure water. The resulting dark red aqueous solution was impregnated on 4.00 g of calcined silica ($SiO_2$, Cabot, M-7D, 200 $m^2/g$, 99.9%+) by successive incipient wetness impregnations. A portion (~ 1 g) of the dried precursor was calcined in air, by heating from room temperature to 773 K at 40 K $min^{-1}$ and held at that temperature for an additional 3 h. Following cooling to room temperature the sample was placed in a snap-cap vial and stored at room temperature. The calcined rhodium metal precursor was either reduced or sulfided *in-situ* as described in section 2.3.3.

*Supported rhodium phosphide ($Rh_2P/SiO_2$)*

A supported rhodium phosphide catalyst ($Rh_2P/SiO_2$) was produced with a theoretical loading of 5 wt% $Rh_2P$ and excess P (P/Rh = 0.75) by impregnating a solution of 0.188 g $RhCl_3 \cdot xH_2O$ (x ≈ 2.9, Johnson Mathey, 99.9%) and 0.0578 g $NH_4H_2PO_4$ (Alfa Aesar, 98.0%) in nanopure water onto 1.50 $SiO_2$. The solution was impregnated onto the silica support as described above, and the resulting impregnated support was placed in a 383 K oven and dried for 1 hour. Impregnations were repeated until all the solution and subsequent washes were transferred onto the support. The catalyst precursor was dried for an additional 24 hours, calcined at 773 for 3 h in air, and stored in a snap-cap vial at room temperature.

Catalyst precursors were reduced using a flow synthesis apparatus shown in Figure 2.1.

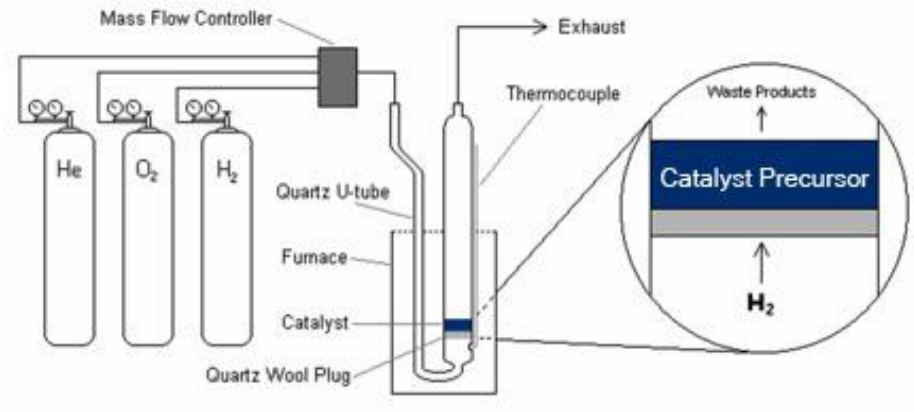


**Figure 2.1 Flow control apparatus used to reduce and passivate catalyst precursors.**

The catalyst precursor (0.05-0.5 g) was placed on a quartz wool plug (~0.1 g) fitted in the base of a quartz U-tube. The U-tube was placed in a ceramic fiber furnace and attached to the flow synthesis apparatus. Gas flows were controlled by a gas flow controller (MKS instruments, Type 1159B) connected to a four channel readout (MKS instruments, Model 247C) and reduction temperature was controlled by a microprocessor temperature controller (Watlow, Series 981) attached to the ceramic furnace. A thermocouple mounted to the U-tube monitored reduction temperature while a second thermocouple placed in the ceramic furnace lid provided thermal over-limit protection.

The calcined rhodium phosphide precursor was reduced using a modified temperature programmed reduction (TPR) protocol described by Gaudette et al.[1] and described below. The sample was degassed with He (Airgass, 99.999%) at a flow rate of 60 mL/min for a minimum of 30 min. Gas flow was changed to $H_2$ (Airgass, 99.999%) at a flow rate of 300 mL/min and the sample was heated from room temperature to 923 K at a rate

of 1 K/min, and then cooled back to room temperature. Once at room temperature, the gas flow was changed back to He flowed at 60 mL/min, and the sample was degassed for 30 min. The reduced sample was then passivated with 1 mol% $O_2$/He (Airgas) flowed at 30 mL/min for 2 h to prevent rapid and deep oxidation of the catalyst when exposed to air. The sample was then collected and transferred to a snap cap vial for storage.

### 2.1.2 Palladium Catalysts

*Supported palladium ($Pd/SiO_2$) and palladium chloride ($PdCl_2/SiO_2$) precursors*

A supported palladium metal catalyst precursor, with a metal loading equivalent to a 5 wt% $Pd_3P/SiO_2$ (4.4 wt% Pd) was prepared by dissolving 0.1599 g of palladium (II) chloride ($Pd(II)Cl_2$, Pressure Chemical) in ~10 mL of nanopure water. The resulting dark orange solution was impregnated on 2.00 g of calcined silica as described above. Approximately 1 g of the dried precursor was calcined by heating from room temperature to 773 K at 40 K $min^{-1}$, held at temperature for 3 h, and then cooled to room temperature. Both the calcined palladium metal precursor and the remaining uncalcined palladium chloride precursor were transferred to separate snap cap vials and stored at room temperature.

*Supported palladium metal ($Pd/SiO_2$)*

Supported palladium metal catalysts ($Pd/SiO_2$) were prepared by *in-situ* reduction of the calcined palladium metal precursor and uncalcined palladium chloride precursor as described in section 2.3.3.

*Supported palladium phosphides ($Pd_xP_y/SiO_2$) – calcined precursors*

A series of palladium phosphide catalysts were synthesized with varying phosphorous to palladium molar ratios (P/Pd = 0.39, 0.79, 1.17, 2.3, 3.5) by successive

incipient wetness impregnations of the silica supported calcined palladium ($Pd/SiO_2$) with an aqueous ammonium hypophosphite ($NH_4H_2PO_2$, Fluka Analytical, ≥97%) solution. Reagent quantities are listed in Table 2.1.

**Table 2.1 Reagent Masses for calcined PdxPy/SiO2 catalysts.**

| P/Pd Molar Ratio | $PdCl_2/SiO_2$ calc. (g) | Pd (g) | $NH_4H_2PO_2$ (g) |
|---|---|---|---|
| 0.39 | 0.5114 | 0.0227 | 0.00698 |
| 0.79 | 0.5001 | 0.0222 | 0.0136 |
| 1.17 | 0.5000 | 0.0222 | 0.0203 |
| 2.3 | 0.4998 | 0.0223 | 0.0397 |

The catalysts were dried in an oven at 341 K for at least 1 h between impregnations, and for 24 h after the final addition. The hypophosphite-based metal precursors were converted to metal phosphide catalysts by temperature program reduction (TPR) as describe above. The maximum TPR temperature was varied (773-973 K) to explore the effect of reduction temperature on phase purity and average crystallite size.

*Supported palladium phosphides ($Pd_xP_y/SiO_2$) – uncalcined precursors*

Several palladium phosphide catalysts were prepared by successive incipient wetness impregnations of the uncalcined palladium precursor ($PdCl_2/SiO_2$) with an aqueous ammonium hypophosphite solution (P/Pd = 0.82 and 2.09). The hypophosphite-based precursors were dried in an oven at 341 K for at least 1 h between each impregnation step, and for 24 h following the final impregnation. The Metal chloride hypophosphite precursors were converted to metal phosphide catalysts by TPR. Similar to the palladium phosphide catalysts prepared from calcined precursors described above, the maximum TPR temperature (773-973 K) and hydrogen flow rates (10 mL/min, 50 mL/min, 100 mL/min) were adjusted as necessary to obtain phase pure materials.

### 2.1.3 Ruthenium Catalysts

*Supported ruthenium chloride ($RuCl_3/SiO_2$) precursors*

A silica-supported ruthenium catalyst precursor, with an Ru loading equivalent to that of a 15 wt % $Ru_2P/SiO_2$ catalyst (10.6 wt% Ru) was prepared by dissolving 0.6989 g of $RuCl_3 \cdot 3H_2O$ (Pressure chemical Co.) in 13 ml of nanopure water. The resulting dark red aqueous solution was impregnated onto 2.00 g $SiO_2$ as previously described. The precursor was dried at 393 K for at least 1 h between impregnations, and 24 h following the final impregnation. The dried dark brown precursor was transferred to a snap cap vial and stored at room temperature.

*Supported ruthenium metal ($Ru/SiO_2$)*

A supported ruthenium metal catalyst was prepared by *in-situ* reduction of the ruthenium chloride precursor ($RuCl_3/SiO_2$) as described in 2.3.11.

*Supported ruthenium phosphides ($Ru_xP_y/SiO_2$) – uncalcined precursors*

A series of ruthenium phosphide catalysts were synthesized with varying phosphorous to ruthenium molar ratios (P/Ru = 0.61, 0.73, 0.86, 1.11, 1.39). The quantities of reagents used are listed in Table 2.2.

**Table 2.2 Reagent masses for uncalcined $Ru_xP_y/SiO_2$ catalysts.**

| P/Ru Molar Ratio | 21.8 wt. % $RuCl_3/SiO_2$ (g) | Ru (g) | $NH_4H_2PO_2$ (g) |
|---|---|---|---|
| 0.61 | 0.5000 | 0.0529 | 0.0265 |
| 0.73 | 0.5002 | 0.0529 | 0.0321 |
| 0.86 | 0.5000 | 0.0528 | 0.0372 |
| 1.11 | 0.5000 | 0.0529 | 0.0483 |
| 1.40 | 0.4951 | 0.0524 | 0.0605 |

Successive incipient wetness impregnations of the uncalcined ruthenium chloride precursor with aqueous ammonium hypophosphite were conducted to prepare the uncalcined hypophosphite precursor. TPR was performed as described above (773 K, 100 mL/min $H_2$) to convert the uncalcined hypophosphite precursor to the ruthenium phosphide catalyst.

## 2.2 Characterization Methods

*X-Ray diffraction*

X-Ray diffraction (XRD) patterns of the catalysts prepared in this research were obtained on a PANalytical X'Pert Pro MRD x-ray diffractometer operating at 45 mV and 40 mA and using a Cu-$K_\alpha$ monochromatic x-ray source (λ = 1.54056 Å). Data were collected over a Bragg angle (2Θ) range of 20-80° with a step size of 0.025°. Dwell time, or time per step, was adjusted from 1.00 to 25.00 s as needed to achieve the desired signal-to-noise ratio. Data files were converted to ASCII format and exported using X'Pert HighScore software. Reference patterns from the JCPDS powder diffraction file database were exported for comparison using X'pert HighScore software. Origin 8.0 software was used to plot both the obtained XRD patterns and reference patterns for phase identification as well as determination of average crystallite size ($D_c$). The average crystallite size was calculated using the Scherrer equation (Equation 2.1), given $K$ = 1, $\lambda$ is the wavelength of diffracted radiation (0.154056 nm), β is the full width at half height in radians, of the diffraction peak observed at Bragg angle 2Θ.

$$D_c = \frac{K\lambda}{\beta \cos\theta} \tag{2.1}$$

Catalyst samples were mounted on a glass microscope slide using a methanol suspension method. Approximately 0.025 g of sample was placed in the center of the slide.

Several drops of methanol were added to create a paste, which was spread uniformly on the slide using a metal spatula. The methanol was then allowed to evaporate, which resulted in an even layer of sample adhered to the slide. The slide was mounted to the instrument using a custom aluminum stage with two sliding brackets. A stage setting of z = 8.380, was used for all measurements.

*Transmission electron microscopy*

Transmission electron microscopy (TEM) images of the catalyst samples were obtained at the Environmental Molecular Science Laboratory (EMSL) user facility of the Pacific Northwest National Laboratory (PNNL). A JEOL 2010 high-resolution transmission electron microscope was used, operating at 200 keV and equipped with a high-brightness, single-crystal LaB6 filament electron source. Samples were mounted on copper grids coated with Formvar or Lacey carbon.

*X-Ray photoelectron spectroscopy*

X-ray photoelectron spectra (XPS) were collected at the EMSL user facility using a Physical Electronics Instruments (PHI) 5000 VersaProbe scanning ESCA microprobe, equipped with a focused monochromatic Al-$K_\alpha$ X-ray (1486.7 eV) source and a spherical section analyzer. Samples were neutralized with low energy electrons and argon ions prior to data collection. All spectra were collected with a pass energy of 23.5 eV, analyzed with VersaProbe XPS V1.3 software, and referenced to the C(1s) peak at 284.5 eV to correct for sample charging.

*CO chemisorption and BET surface area*

A Micromeritics PulseChemisorb 2700 instrument was used to measure CO chemisorption capacities and BET surface areas, following procedures described by Gaudette et al.[1] Approximately 0.1 g of catalyst was placed in a quartz U-tube which was attached to the instrument. The tube was flushed with 60 mL/min He for 30 min, and then subjected to either $H_2$ or $H_2S/H_2$ pretreatment. Typically, the catalyst was heated to 650 K at 6 K/min under 60 mL/min $H_2$, and held for 2 h; then it was heated to 673 K under 60 mL/min He and held for 1 h. The sample was cooled to room temperature and then submerged in an ice water bath to cool the catalyst to 273 K. A portion of the CO (Messer) analysis gas line tubing was submerged in a pentane slush (~142 K) to remove metal carbonyl impurities from the gas, as well as a dewar of liquid $N_2$ (~77 K) to condense contaminant vapors.

To calibrate the amount of CO gas in each pulse, the sample tube was bypassed and 5 s pulses of CO were delivered directly to the detector, while maintaining a 45 mL/min flow of He. The area of the peak resulting from the gas flow was recorded as the area of a single pulse. For the measurement, CO was pulsed over the sample for 5 s in 1 min intervals, maintaining 45 mL/min He, until peak areas from successive pulses became consistent. The total peak area from the measurement was recorded as the non-adsorbed peak area. The ice bath was then replaced with a furnace, heating the sample to 673 K, and the desorbed peak area was recorded by the detector.

Chemisorption capacities were obtained by subtracting the non-adsorbed peak area from the product of the peak area per pulse and the number of pulses measured, as shown in equation 2.2. This value, the adsorbed peak area, was multiplied by a factor converting

peak area per pulse to µmol of gas per pulse (equation 2.3). Dividing by the final catalyst weight in grams gives the chemisorption capacity in µmol/g. The values obtained using the adsorbed and desorbed peak areas, as shown in equations 2.4 and 2.5, were averaged to determine the final chemisorption capacity.

$$Adsorbed\ Area = (\#\ of\ pulses) * (peak\ area) - NAPA \qquad (2.2)$$

$$n = \frac{PV}{RT} = \frac{(1\ atm)*(101*10^{-6}L)}{\left(0.082058\frac{L*atm}{mol*K}\right)*298\ K} = 4.131\ \mu mol\ probe\ gas \qquad (2.3)$$

$$CO\ chemisorption\ capacity = \frac{(Adsorbed\ Area)*\frac{\mu mol\ CO}{pulse\ area}}{g\ catalyst} \qquad (2.4)$$

$$Desorbed\ CO\ chemisorption\ capacity = \frac{(Desorbed\ Area)*\frac{\mu mol\ CO}{pulse\ area}}{g\ catalyst} \qquad (2.5)$$

BET surface areas were measured as follows. Approximately 0.1 g of catalyst was placed in a quartz U-tube, which was attached to the instrument. The tube was flushed with 60 mL/min He for 30 min, then heated to 673 K under 43 mL/min He for 2 h. After cooling the sample to room temperature, 28.6 mol% $N_2$/He was flowed at 43 mL/min directly to the detector (bypassing the sample) and the amount of gas flow was calibrated by injecting gaseous $N_2$ into the $N_2$/He gas stream in volumes of 0.2, 0.6 and 1.0 mL using a gas tight syringe. The resulting peak areas were used to find a linear regression equation relating peak area to volume of $N_2$ in mL. For the measurement, 43 mL/min $N_2$/He was flowed over

the sample, and the tube was submerged in liquid nitrogen. The resulting peak area was recorded as $N_2$ deficiency in the $N_2$/He mix, corresponding to the amount of adsorbed $N_2$. The tube was then submerged in water at ~303 K, and the resulting peak area was recorded as $N_2$ excess in the $N_2$/He mix, corresponding to the amount of desorbed $N_2$. The values were averaged and substituted into the linear regression equation described above to give the volume of $N_2$ adsorbed/desorbed. This amount was multiplied by 2.82 $m^2$/mL (BET factor derived from the ideal gas law), and then divided by the final catalyst mass (in grams) to yield the surface area in $m^2$/g, using equation 2.6.

$$BET\ surface\ area = \frac{(Volume\ \ N_2\ \ adsorbed)(2.82\ \ m^2 N_2 / mL)}{g\ \ catalyst} \qquad (2.6)$$

*Sulfur and Carbon Analyses*

Sulfur and carbon analyses of catalyst samples were carried out using a LECO SC-144DR Sulfur and Carbon Analyzer. To prepare a catalyst sample, approximately 0.15 g of the catalyst was degassed in 50 mL/min He for 15 min at room temperature. The flow was switched to 60 mL/min $H_2$ and the sample was heated to 573 K in 1 h and held at this temperature for 2 h. The sample was then cooled to room temperature in flowing $H_2$. After cooling, the gas feed was switched to 60 mL/min of 3.0 mol% $H_2S/H_2$. The sample was then heated from room temperature to 573 K in 1 h and held at this temperature for 2 h. The gas feed was then changed to 50 mL/min He and the sample held at 573 K for 1 h. After degassing, the sample was cooled to room temperature and passivated for 2 h in 60 mL/min of 1.0 mol% $O_2$/He. The sulfur and carbon analyses were carried out as follows. Approximately 0.1000 g of catalyst was transferred into a ceramic boat. The ceramic boat

was then loaded into a furnace where the sample was combusted in an oxygen-rich environment at ~1625 K for 3 min. Combusted carbon ($CO_2$) and sulfur ($SO_2$) that evolved from the catalyst sample was quantified via IR detection and reported as wt% C and S. Sulfur analysis was also performed on catalyst samples following HDS activity measurements.

## 2.3 Catalytic Activity Measurements

### 2.3.1 Hydrodesulfurization (HDS) activity

*HDS Reactor System*

Two identical, continuous downward flow, fixed-bed reactor systems were assembled to mimic conditions typical of industrial HDS processes (Figure 2.2).

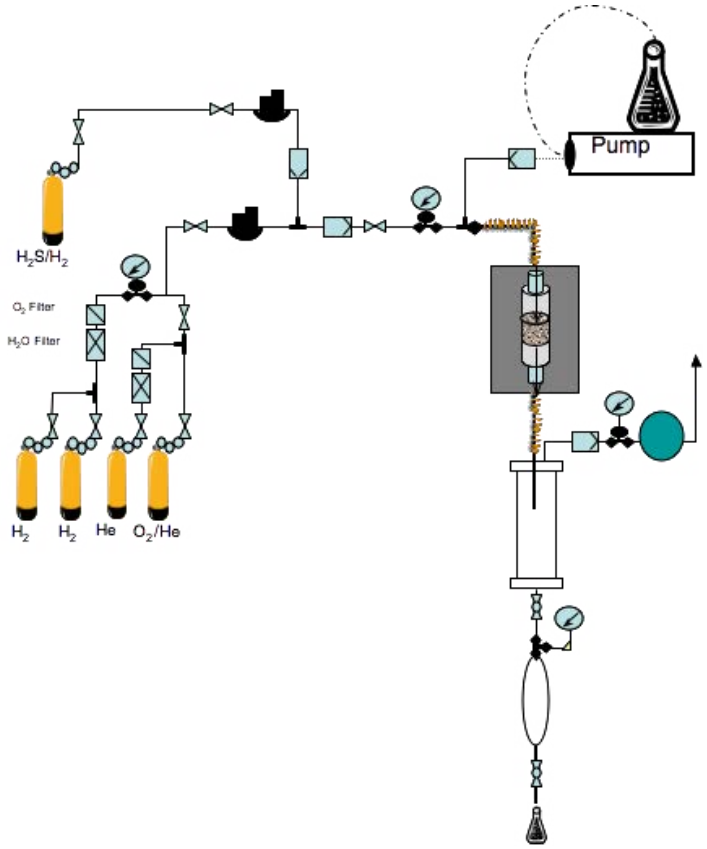


**Figure 2.2 Downward flow reactor system for HDS activity measurements.**

Similar to conditions described by Egorova et al.[2] and Jimenez-Lopez et al.[3], the reactors were operated at 3.1 MPa as set by a backpressure regulator (Swagelok) and within a temperature range of 498-673 K during HDS activity measurements. The gas flow of the carrier gases was controlled by mass flow controllers (Brooks, 5850S) interfaced to a personal computer running Brooks SmartFlow software. The internal reactor temperature was monitored by an axial mounted Type K thermocouple (Omega) in direct contact with the catalyst bed, and controlled by a 2000 watt clamshell furnace (Watlow) connected to a programmable temperature controller (Watlow, Series 982). Stock feed solutions were injected at 5.4 mL/hr using a Gilson Series I high performance piston pump equipped with a 316 stainless steel pump head. Heating tape (Duo Tape, HTS/Amptek) wrapped around the reactor inlet vaporized the liquid feed prior to reaching the catalyst bed.

*Sample Preparation*

The catalyst sample powder (~0.2 g) was pressed into 1 cm diameter wafers, approximately 1 mm thick, using a stainless steel die-set and hydraulic press (Preco Inc., PA7) exerting 6000 pounds platen pressure. The obtained catalyst wafers were then crushed into flakes. Using stainless steel wire sieves (Fisher Scientific), 0.1500 g of catalyst flakes, sized 16-20 mesh, were collected and diluted to 5 mL with +16 mesh quartz flakes (Aldrich, 99.9%) to mitigate flow problems described by Bej et al.[4] A stainless steel reactor tube (Autoclave Engineers, 106A-2454, i.d. 11.2 mm) was used for the body of the HDS test reactor. The catalyst bed was situated between two layers of quartz wool, and supported on top and bottom by 3 mm dia. Pyrex® (Corning, 7740) glass beads. An axially mounted Type K thermocouple (Omega, KMQ3166SS-062U-24) was used to directly monitor the

catalyst bed temperature. Following HDS testing, the catalyst was separated from the quartz flakes using the wire mesh sieves.

*Catalyst Pretreatment*

All catalyst samples were pretreated *in situ* at atmospheric pressure prior to HDS testing by one of three methods: degas-only, reduction, or sulfidation pretreatment. All catalysts were subjected to the helium degas pretreatment in which the reactors were degassed at room temperature with He gas (Praxair, 99.999%) flowed at 60 mL/min for 30 min. Catalyst samples subjected to the helium degas-only pretreatment would then proceed directly to testing in HDS activity conditions. Catalyst samples subjected to the sulfidation pretreatment were degassed in He, heated from room temperature to 650 K (5.9 K/min) in a 60 mL/min flow of either 3 mol % $H_2S/H_2$ (Airgas) or 10 mol % $H_2S/N_2$ (Airgas), depending on the catalyst, and held at 650 K for 2 h. Following the pretreatment, the catalysts were cooled back to room temperature. For catalysts subjected to the reduction pretreatment, samples were degassed in He, heated to 650 K (5.9K/min) in a 60 mL/min flow of $H_2$ (Praxair, 99.999%), held at 650 K for 2 h, and cooled to room temperature.

*HDS Activity Tests*

Following pretreatment, the reactor was pressurized to 3.1 MPa with $H_2$ (Airgas, 99.999%) at 100 mL/min. Once the operating pressure was reached, the temperature was raised to a starting temperature in the range of 498-548 K, depending on the catalyst being tested. Three types of HDS activity experiments were conducted to fully assess the performance of each catalyst.

*Activity vs. Temperature*

For an initial assessment of HDS activity, a catalyst was subjected to a step-wise temperature ramp and HDS activity was monitored at each temperature increment, and was conducted as follows. Once the reactor operating temperature was reached (498-548 K), a stock feed consisting of 3000 ppm dibenzothiophene (DBT, Acrōs, 99%) and 500 ppm dodecane (Matheson Coleman & Bell) dissolved in decalin (Sigma Aldrich, ≥99%) was injected into the flow of 100 mL/min $H_2$. Reactor activity was allowed to stabilize for a minimum of 3 h before liquid samples were collected. Following stabilization, the initial reactor effluent was collected and discarded. Four additional effluent samples were then collected at 30 min intervals and analyzed by GC as described below. Once the fourth sample was acquired, the reactor temperature was increased by 25 K, and the sampling protocol was repeated as described above. During these HDS activity measurements, each catalyst was subjected to a minimum of five temperature increments.

*100 h HDS Activity Measurement*

A second type of HDS experiment was conducted to investigate the HDS activity over the course of 100 h at a constant temperature. When the reactor reached the selected operating pressure and temperature, a similar stock feed as described above was injected into a 100 mL/min flow of $H_2$. Sampling began 1 h after introduction of the stock feed and samples were taken every 1-3 h (6-8 h overnight) over the course of 100 h. Reactor effluent samples were analyzed by GC as described below.

*Activity vs. $H_2S$ Partial Pressure*

An experiment to examine the effect of $H_2S$ partial pressure on HDS activity was conducted for several of the most promising catalysts. HDS activity was measured while co-feeding increasing amounts of $H_2S$. Dimethyldisulfide (DMDS, Aldrich, 99.0%+), which readily decomposes under experimental conditions to produce $H_2S$ (Equation 2.7), was added to the standard liquid feed in amounts of 1100 (1kPa $H_2S$), 3200 (3kPa $H_2S$), 10700 (10 kPa $H_2S$), and 53000 ppm DMDS (50 kPa $H_2S$).

$$CH_3SSCH_3\,(g) + 3H_2\,(g) \rightarrow 2CH_4\,(g) + 2H_2S\,(g) \qquad (2.7)$$

The reactor system was allowed to equilibrate for 3 h after changing solutions with different DMDS concentrations. After the initial sample of reactor effluent was discarded, four additional samples were taken at 1 h intervals and analyzed by gas chromatography as described below.

*Reactor Shutdown and Catalyst Recovery*

After completion of an HDS measurement, the flow liquid feed was stopped while the $H_2$ gas flow and reactor temperature were maintained for 1 h. The reactor was then cooled to room temperature, reduced to atmospheric pressure, and then purged with He flowed at 60 mL/min for 30 min. The system was then opened, and allowed to sit for a minimum of 3 h to permit the slow exposure of the tested catalyst to ambient air. The catalyst sample was then removed from the reactor and separated from the quartz flakes using a 16 mesh wire sieve (Fischer). The collected catalyst flakes were dried with compressed air to evaporate residual stock feed solution and ground to a powder using a

mortar and pestle. XRD and sulfur analysis were performed on the HDS-tested catalyst powder.

*HDS Activity and Selectivity Analyses*

The reactor effluent was collected in 1.5 mL gas chromatography (GC) vials (Restek) and analyzed offline using an Agilent 6890N gas chromatograph equipped with an HP-5 column (50 m X 0.320 i.d.), 7683B automatic sample injector, and a flame ionization detector. A split injection (39.9:1 ratio) method with an inlet flow of 108 mL/min was used. Helium (2.7 mL/min) served as the carrier gas. The GC inlet and detector temperatures were maintained at 250 and 260 °C, respectively, throughout the protocol. The initial column temperature was set to 120 °C and increased to 140 °C (10 °C/min) following a 3 µL sample injection. The column temperature was held at 140 °C for 2 min then heated to 250 °C (15 °C/min) to complete the analysis method.

The quantification of the reactor effluent was performed using a six point internal standard calibration curve prepared for DBT and each of the three major products (biphenyl, cyclohexyl benzene, and bicyclohexane). Solutions containing 3000, 1500, 750, 325, and 123 ppm of each analyte dissolved in a 500 ppm dodecane / decalin solution served as standards. A GC trace of the 3000 ppm standard solution is shown in Figure 2.3.

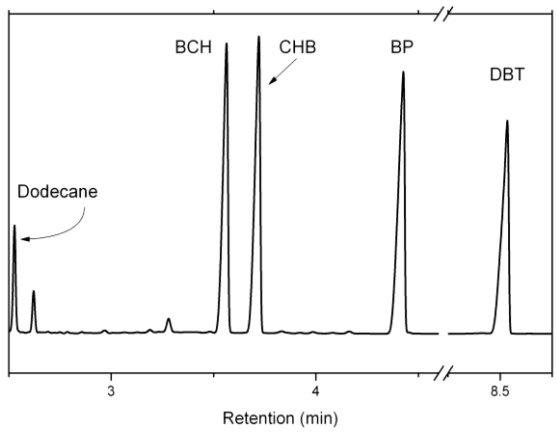


**Figure 2.3 GC trace of a 3000 ppm product standard solution.**

The analyte signal was normalized to the dodecane internal reference signal (to account for slight sample size variation) and reported as the analyte response factor (rf). A regression analysis of the resulting reference plot of response factor versus analyte concentration was used to quantify the overall DBT activity and product distribution in each sample, and is shown in Figure 2.4. The calculated response factors for each analyte are show in Table 2.3.

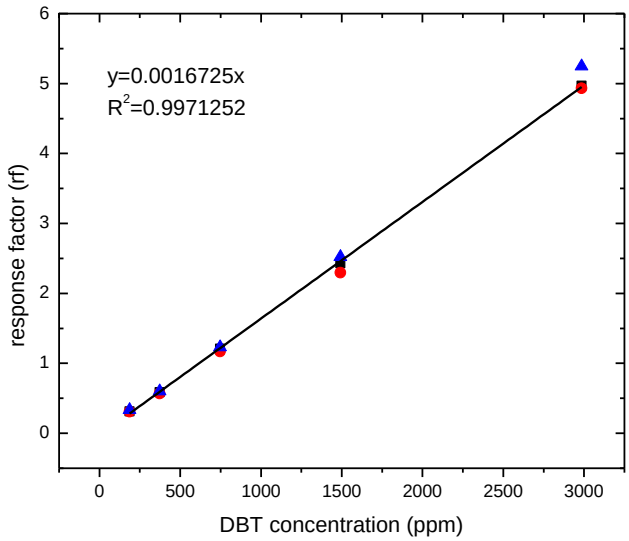


**Figure 2.4 Calibration curve used to quantify DBT concentrations in reactor effluent.**

**Table 2.3 Response factors calculated from analyte calibration curves.**

| Compound | Retention Time (min) | Area at 600 ppm | Response Factor $\left(\frac{\frac{area\ of\ analyte}{avg.\ C12\ area}}{conc.\ analyte}\right)$ |
|---|---|---|---|
| Dodecane (C12) | 2.54 | 630 | -- |
| Bicyclohexane (BCH) | 3.5 | -- | 0.001873 |
| Cyclohexyl benzene (CHB) | 3.6 | -- | 0.001866 |
| Biphenyl (BP) | 4.4 | -- | 0.001989 |
| Dibenzothiophene (DBT) | 8.5 | -- | 0.001673 |

### 2.3.2 Hydrodeoxygenation (HDO) activity

*HDO Reactor System*

Furan HDO measurements were performed using an atmospheric pressure flow reactor system, similar to the HDS system described by Sawhill,[5] and shown in Figure 2.5.

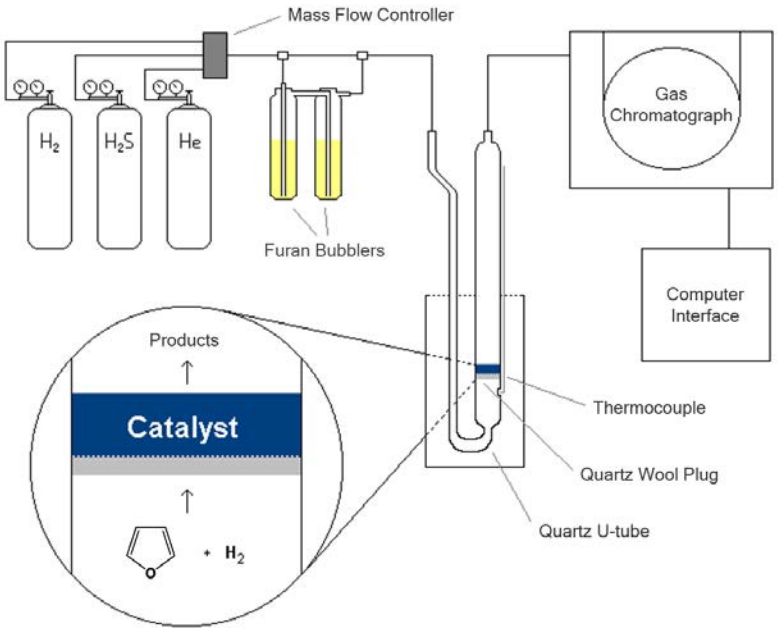


**Figure 2.5 Flow reactor used for HDO testing.**

Glass bubblers filled with furan (Aldrich, 99+%) were cooled to 250 K by a recirculating refrigerated bath (Thermo Haake, C30-P) filled with 50:50 (v/v) ethylene glycol (Prestone) and water solution. Gas flow through the system was governed by a mass flow controller (MKS Instruments, 1159B) connected to a four channel readout (MKS, Type 247C). The reaction temperature was monitored by a Type K thermocouple fitted into a notch in the U-tube, and was controlled by a ceramic fiber furnace (Watlow) connected to a programmable temperature controller (Omega, Type CN-2011K). The reactor effluent was sampled at 1 h intervals and analyzed on-line by a gas chromatograph (GC) equipped with a pneumatic sampling valve (Valco), both of which were controlled by a personal computer running ChemStation software.

*HDO Activity Measurements*

HDO activity measurements were conducted as follows. Approximately 0.1000 g of catalyst was loaded into a quartz U-tube and supported by ~0.1 g of quartz wool. The sample was degassed in a 50 mL/min He flow for 30 min. The catalyst was then either reduced in-situ with $H_2$ or heated directly to HDO conditions. For the reduction pretreatment, the gas flow was changed to $H_2$ at 50 mL/min. The catalyst sample was heated from room temperature to 650 K in 1 h and held at this temperature for an additional 2 h. Following the pretreatment, the $H_2$ gas was flowed at 50 mL/min through the two in-series furan bubblers cooled to 250 K. The resulting furan/$H_2$ mixture (8.2 mol % furan) was then passed through a quartz U-tube containing the catalyst supported on quartz wool. The U-tube and catalyst were heated from 650 to 673 K in 5 min. GC sampling began once the catalyst reached 673 K, and continued at 1 h intervals for 48 h. For catalyst

samples not subjected to the reduction pretreatment, the gas flow was changed from He to 50 mL/min $H_2$ saturated with furan at 250 K, as described above. The catalyst was heated from room temperature to 673 K in 15 min. GC sampling began once the temperature reached 673 K and continued for 48 h as previously described.

*Furan HDO Activity and Selectivity Analyses*

Furan HDO activities are reported in units of nanomol of furan converted per gram of catalyst per second (nmol/g cat/s). The relative peak area of furan, obtained from integrating the reaction effluent GC trace, was converted to percent furan converted. Antoine coefficient values used to the calculate the furan vapor pressure at 250 K were obtained from data provided by Yaws and Yang.[6] Based on a furan vapor pressure of 61.9 mm Hg at 250 K (equation 2.8) and a 50 mL/min reactor flow, a furan flow rate of 3030.2 nmol/s was calculated (equation 2.9). Dividing the product of furan flow rate and percent furan converted by the mass of catalyst used in the experiment resulted in the HDO activity as calculated below (equation 2.11).

$$Furan\ Vapor\ Pressure\ (at\ 250\ K) = 10^{6.973-\left(\frac{1060.85}{204.75}\right)} = 61.62\ mmHg \tag{2.8}$$

$$mol\ \%\ Furan = \frac{66.62\ mmHg}{760\ mmHg} \times 100 = 8.15\ \%\ Furan \tag{2.9}$$

$$Molar\ Flow\ Rate = \frac{1\ atm \times 50\frac{mL}{min}}{0.0821\frac{L\ atm}{K\ mol} \times 273\ K} \times \left(\frac{1L}{1000mL}\right) = 0.00223\frac{mols}{min} \tag{2.10}$$

$$Furan\ Flow\ Rate = \left(0.00223\frac{mol}{min}\right) \times \left(\frac{10^9\ nmols}{mol}\right) \times \left(\frac{min}{s}\right) \times\ 0.815 = 3030.2\frac{nmol}{s} \quad (2.11)$$

HDO product concentrations were determined using a single-point response calibration for each of the major products formed (propane, butane, trans-2-butene, 1-butene, cis-2-butene). The response curves, with the exception of propane, were obtained by flowing a reference gas of known concentration through the HDO apparatus. Several GC samples were taken of the reference gas and the observed GC peaks were integrated with ChemStation software. Regression analysis was then preformed on the resulting response area versus product concentration to provide the single point calibration used to calculate product concentrations. The response for propane was calculated using the response of butane, and multiplying it by the mass percent of propane to butane (44.1 g/mol/58.2 g/mol). The product responses are shown in Table 2.4.

**Table 2.4 GC calibration for HDO product analysis.**

| Compound | Retention Time (min) | Concentration (ppm) | Response |
|---|---|---|---|
| Propane | 1.0-1.3 | -- | 0.00531 |
| Butane | 1.9-2.2 | 1000 | 0.00700 |
| trans-2-butene | 4.7 | 10300 | 0.00633 |
| 1-butene | 5.0 | 1000 | 0.00632 |
| cis-2-butene | 6.2 | 9670 | 0.00709 |

## References

1. Gaudette, A. F.; Burns, A. W.; Hayes, J. R.; Smith, M. C.; Bowker, R. H.; Seda, T.; Bussell, M. E., Mossbauer spectroscopy investigation and hydrodesulfurization properties of iron-nickel phosphide catalysts. *J. Catal.* **2010,** *272* (1), 18-27.

2. Egorova, M.; Prins, R., Mutual influence of the HDS of dibenzothiophene and HDN of 2-methylpyridine. *J. Catal.* **2004,** *221* (1), 11-19.

3. Jimenez-Lopez, A.; Cecilia, J. A.; Infantes-Molina, A.; Rodriguez-Castellon, E., The Influence of the Support on the Formation of Ni(2)P Based Catalysts by a New Synthetic Approach. Study of the Catalytic Activity in the Hydrodesulfurization of Dibenzothiophene. *J. Phys. Chem. C* **2009,** *113* (39), 17032-17044.

4. Bej, S. K.; Dabral, R. P.; Gupta, P. C.; Mittal, K. K.; Sen, G. S.; Kapoor, V. K.; Dalai, A. K., Studies on the performance of a microscale trickle bed reactor using different sizes of diluent. *Energy Fuel* **2000,** *14* (3), 701-705.

5. Sawhill, S. J. Transition metal phosphide catalysts for hydrodesulfurization. Master's Thesis, Western Washington University, Bellingham, 2003.

6. Yaws, C. L.; Yang, H. C., To Estimate Vapor-Pressure Easily. *Hydrocarb. Process* **1989,** *68* (10), 65-68.

# Chapter 3. Results

## 3.1 X-ray diffraction (XRD)

X-ray diffraction (XRD) patterns were collected to characterize the crystallite phases present in the silica-supported catalysts prepared in this research. XRD patterns of the prepared catalysts were compared to reference patterns obtained from the JCPDS database[1] to confirm crystallite phase purity and to determine average crystallite sizes using the Scherrer equation (Equation 2.1).

### 3.1.1 Rhodium Catalysts

*Supported rhodium metal ($Rh/SiO_2$)*

Figure 3.1 shows the XRD pattern of a supported rhodium metal catalyst prepared by reduction of a $Rh(NO_3)_3/SiO_2$ precursor in $H_2$. Comparison of the collected pattern with a rhodium metal reference pattern (card #00-005-0685)[1] confirms the synthesis of a phase pure $Rh/SiO_2$. Using the Scherrer equation and the major diffraction peak at 41°, an average crystallite size was calculated to be ~ 6 nm.

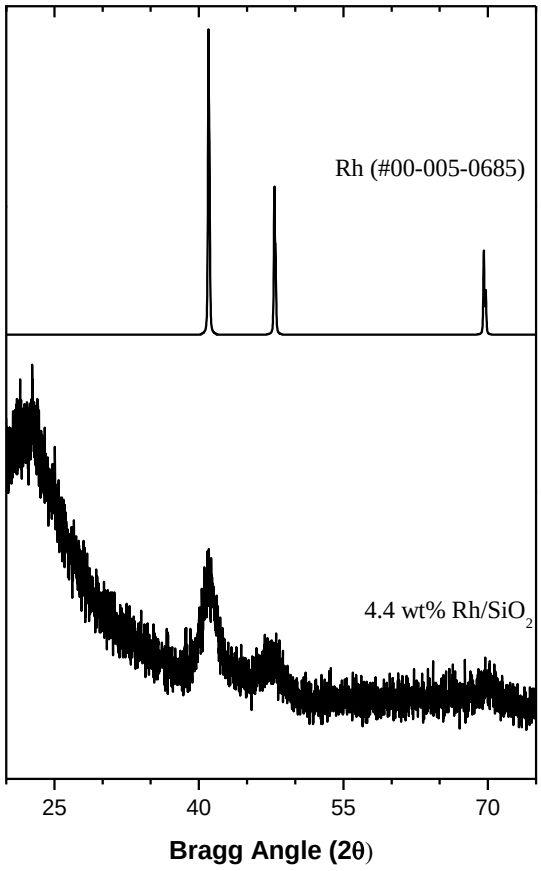


**Figure 3.1 XRD pattern of a 4.4 wt% $Rh/SiO_2$ catalyst.**

*Supported rhodium phosphide ($Rh_2P/SiO_2$)*

The XRD pattern of a 5 wt% $Rh_2P/SiO_2$ catalyst is shown in Figure 3.2. Comparison of the obtained pattern with the $Rh_2P$ reference pattern (#00-002-1299)[1] indicates phase pure $Rh_2P$ was produced. An average crystallite size was calculated to be 7 nm using the Scherrer equation and the diffraction peak at 46.9°.

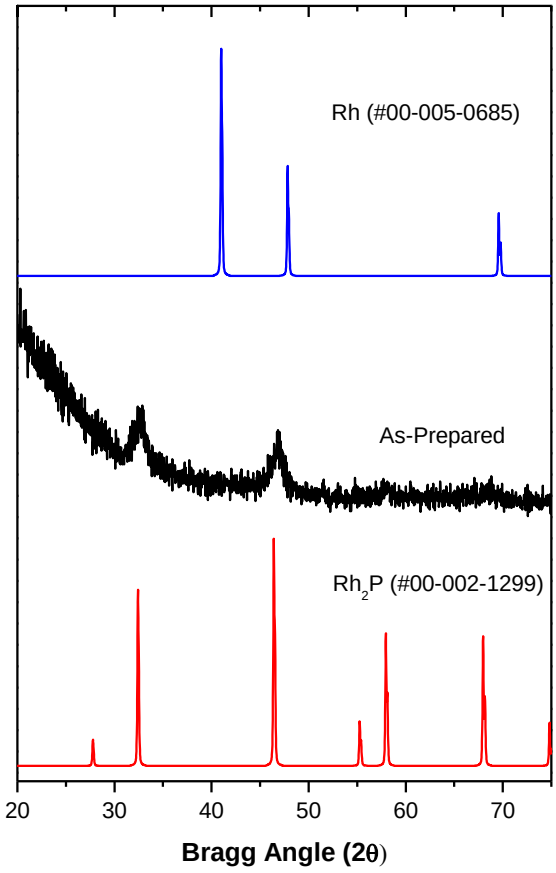


**Figure 3.2 XRD pattern of a 5 wt% $Rh_2P/SiO_2$ catalyst.**

### 3.1.2 Palladium Catalysts

*Supported palladium metal ($Pd/SiO_2$)*

A phase pure silica supported palladium oxide precursor, shown in Figure 3.3, was prepared by calcination of a supported palladium chloride precursor. The oxidic precursor was either reduced in $H_2$ to produce a supported palladium metal catalyst, or impregnated with hypophosphite solutions to give the precursors of supported palladium phosphide catalysts.

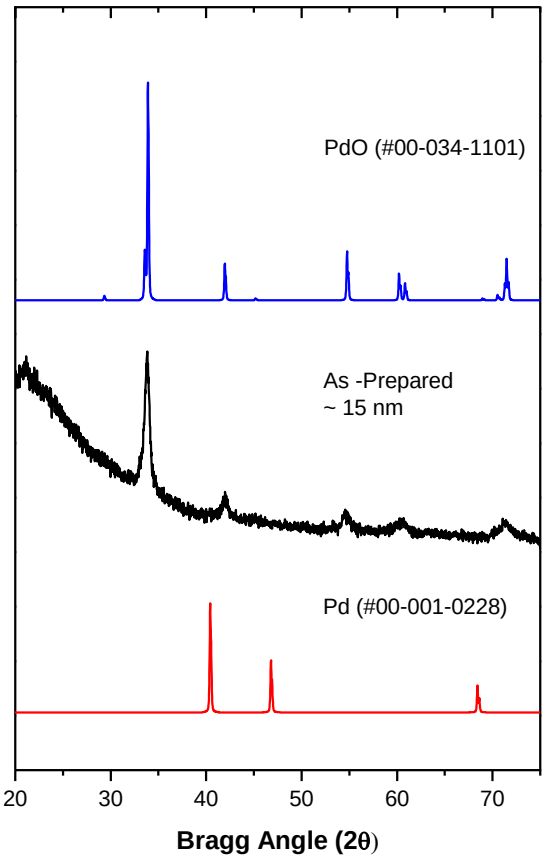


**Figure 3.3 XRD of 5 wt% $PdO/SiO_2$.**

The average crystallite size was calculated to be ~ 15 nm using the Scherrer equation and the diffraction peak observed at 33.0°.

*Supported palladium phosphides ($Pd_xP_y/SiO_2$) – calcined precursors*

The XRD patterns of a 5 wt% $Pd_xP_y/SiO_2$ catalyst, synthesized using a P/Pd molar ratio of 0.39, and reduced at two different temperatures, are shown in Figure 3.4.

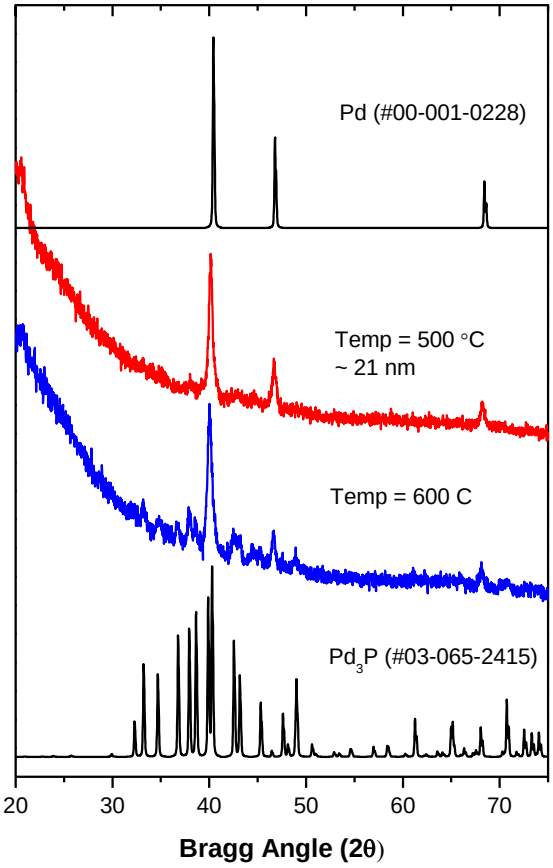


**Figure 3.4 XRD pattern of 5 wt% $Pd_xP_y/SiO_2$ synthesized from P/Pd = 0.39 molar ratio.**

Reduction of the precursor at 500 °C yielded primarily Pd metal, with a minor $Pd_3P$ phase indicated by the peaks at 38.2 and 42.8°. Increasing the reduction temperature to 600 °C resulted in an increase in $Pd_3P$ crystallites, but not a phase pure product, as seen by the

presence of a Pd peak at 46.6°. Additionally, as the $Pd_3P$ content present increased, the large peak observed at 40° became more of an overlapped double peak, rather than the single peak characteristic of palladium metal. Using the Scherrer equation, the average crystallite size was calculated to be 21 nm.

As seen in Figure 3.5, reduction of a 5 wt% $Pd_xP_y/SiO_2$ catalyst, synthesized using a P/Pd molar ratio of 0.79, at 500° C produced a $Pd/SiO_2$ catalyst with a minor $Pd_3P$ impurity.

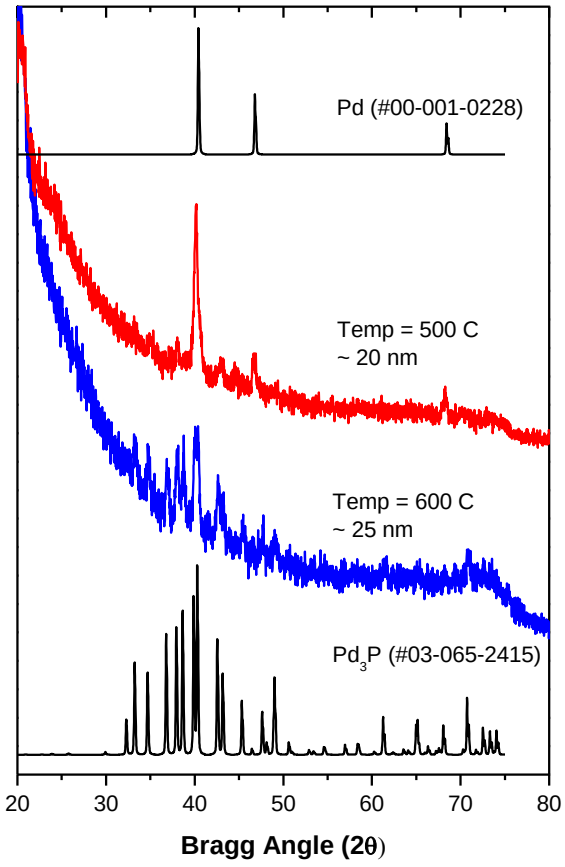


**Figure 3.5 XRD pattern of several 5 wt% $Pd_xP_y/SiO_2$ catalysts synthesized with a P/Pd mole ratio of 0.79.**

Reduction at 600 °C resulted in an almost phase pure $Pd_3P/SiO_2$ catalyst, as the small peak of Pd metal at 46.6° became difficult to distinguish from the baseline and the large peak

observed at 40° became a more defined double peak. Using the Scherrer equation, an average crystallite size was calculated to be ~ 20 nm for the $Pd/SiO_2$ catalyst, and 25 nm for the $Pd_3P/SiO_2$ catalyst.

Phase pure $Pd_3P/SiO_2$ was prepared from a of 5 wt% $Pd_xP_y/SiO_2$ precursor with a 1.17 P/Pd molar ratio by reduction at 550 °C, as shown in Figure 3.6.

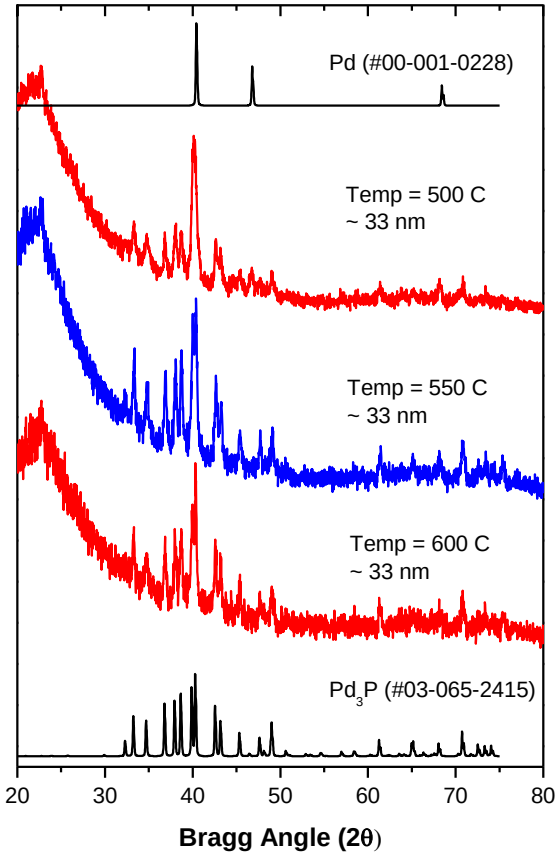


**Figure 3.6 XRD patterns of several 5 wt% $Pd_xP_y/SiO_2$ catalysts synthesized with a P/Pd mole ratio of 1.17.**

Similar to the other precursors synthesized with lower P/Pd ratios, reduction at temperatures less than 550 °C resulted in slight Pd impurities. However, once reduced at 550 °C, phase purity can be confirmed by the presence of a double peak at 40° and the

absence of the Pd peak at 46.6°. Higher reduction temperatures do not seem to affect crystallite purity or size. Using the Scherrer equation, the average crystallite size for phase pure 5 wt% $Pd_3P/SiO_2$ was calculated to be 33 nm.

The XRD of a 5 wt% $Pd_xP_y/SiO_2$ catalyst, synthesized using a 2.3 P/Pd molar ratio, is shown in Figure 3.7.

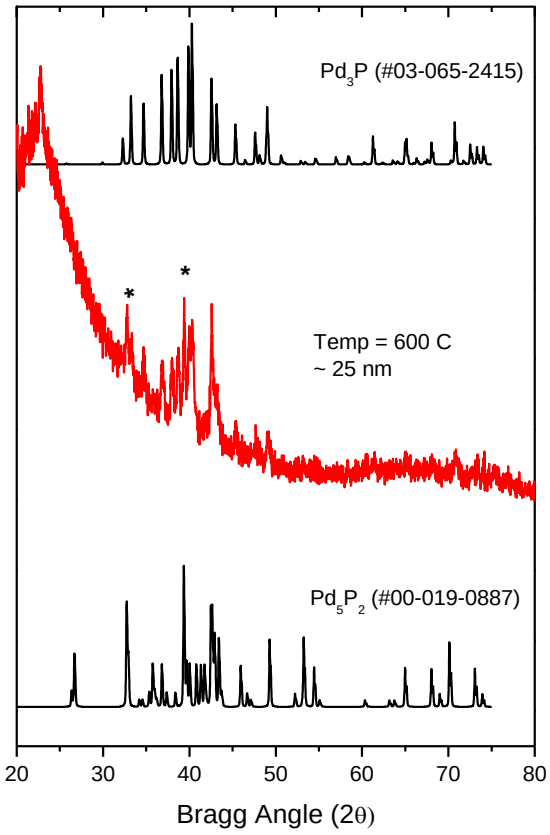


**Figure 3.7 XRD pattern a 5 wt.% $Pd_xP_y/SiO_2$ catalyst prepared from a precursor with a P/Pd mole ratio of 2.3.**

Comparison of the XRD pattern with other palladium phosphide reference patterns reveals a mixture of both $Pd_3P$ and $Pd_5P_2$ phases, with the $Pd_5P_2$ impurity noted using the * symbol.

The average $Pd_5P_2$ crystallite size, calculated using the Scherrer equation, was determined to be about 25 nm.

A series of 5 wt% $Pd_xP_y/SiO_2$ catalysts were prepared using the oxidic precursor having a mole ratio of P/Pd=3.5. Various $H_2$ flow rates during reduction were investigated and the XRD patterns of the resulting samples are shown in Figure 3.8.

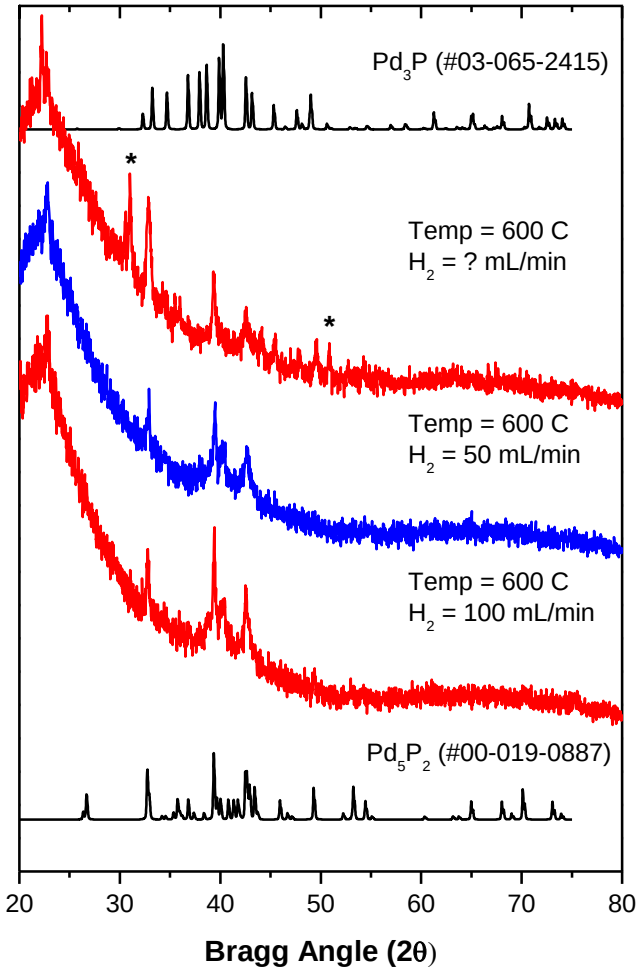


**Figure 3.8 XRD patterns of several 5 wt% $Pd_xP_y/SiO_2$ catalyst synthesized with a P/Pd mole ratio of 3.5.**

Initially, phase pure $Pd_5P_2$ was produced using a $H_2$ flow rate of 100 mL/min. In one experiment, the flow apparatus become partially clogged during a reduction, resulting in a

very low $H_2$ flow, and the XRD pattern revealed a mixture of $Pd_5P_2$ and some other impurity, as indicated by the * symbol in Figure 3.8. Comparison with various palladium phosphide reference patterns identified the impurity as $PdP_2$, as shown in Figure 3.9. Average particle size of the phase pure product was calculated to be ~20 nm.

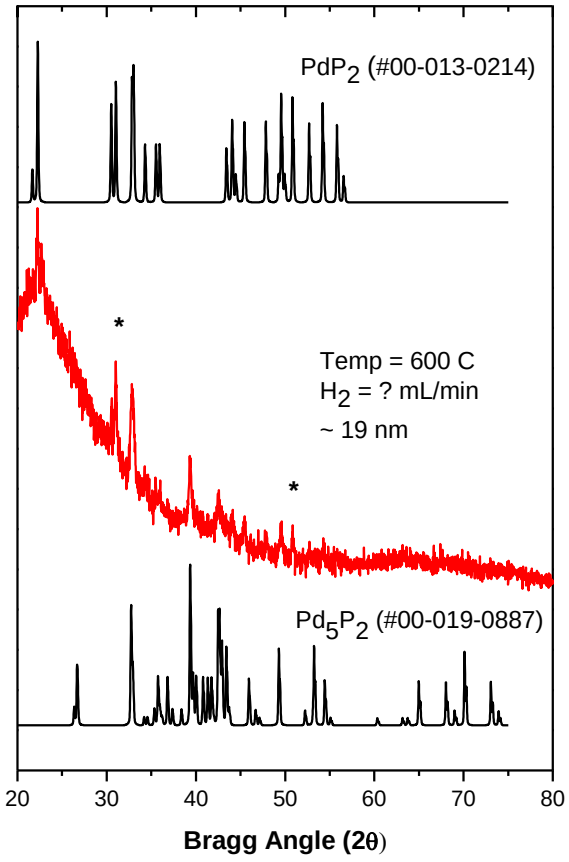


**Figure 3.9 XRD pattern of a 5 wt% $Pd_xP_y/SiO_2$ catalyst synthesized with a P/Pd mole ratio of 3.5.**

An XRD pattern of an HDS-tested 5 wt% $Pd_3P/SiO_2$ catalyst produced from a calcined precursor having a P/Pd mole ratio of 1.17 is shown in Figure 3.10. Comparison of the post-HDS pattern with a $Pd_3P$ reference pattern, as well as the as-prepared pattern, reveals no loss in catalyst phase purity or change in average crystallite size.

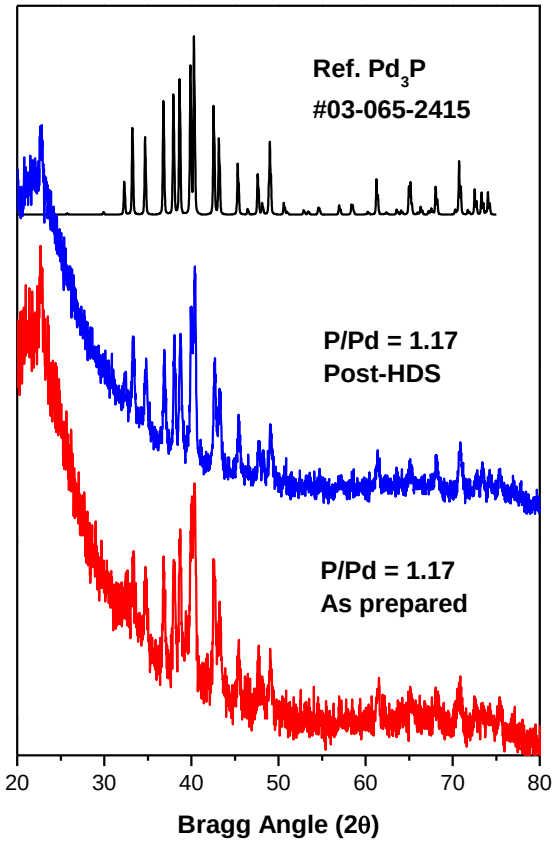


**Figure 3.10 XRD pattern of a calcined 5 wt% $Pd_3P/SiO_2$ catalyst, synthesized from a calcined precursor having a P/Pd molar ratio of 1.17, before and after DBT HDS testing.**

*Supported palladium phosphides ($Pd_xP_y/SiO_2$) – uncalcined precursors*

Several supported phosphide catalysts were produced by hypophosphite impregnation of uncalcined palladium chloride precursors and subsequent reduction. Figure 3.11 shows the XRD patterns of a series of catalysts synthesized from a palladium

chloride precursor having a P/Pd molar ratio of 0.82. Similar to the XRD patterns for catalysts synthesized from calcined precursors, the reduction of the uncalcined hypophosphite precursor at 500° C resulted in a mixture of palladium metal and $Pd_3P$ phases on the silica support. Reduction at higher temperatures produced phase pure $Pd_3P$, as is evident by the large overlapped peaks present at 40°.

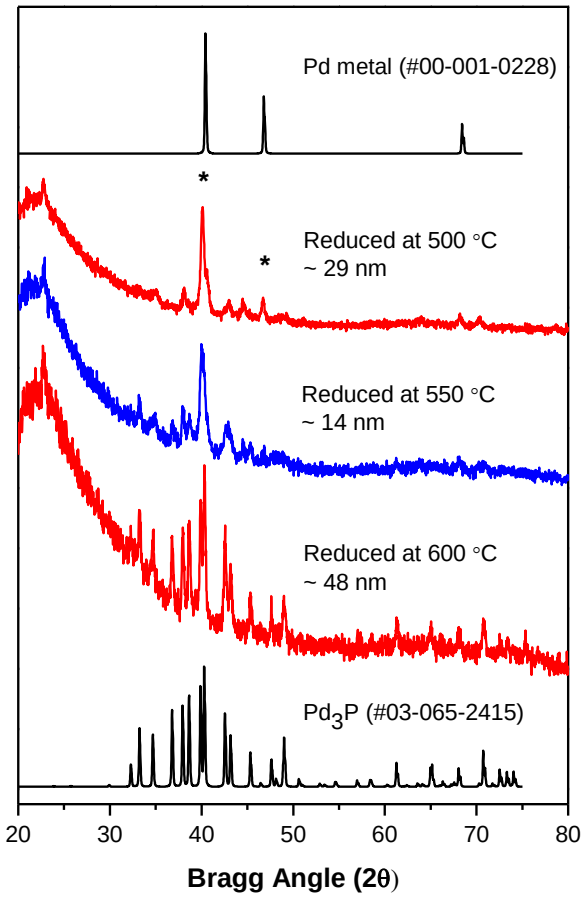


**Figure 3.11 XRD pattern of a 5 wt% $Pd_xP_y/SiO_2$ catalyst synthesized with a P/Pd mole ratio of 0.82.**

Several attempts were made to synthesize phase pure $Pd_5P_2/SiO_2$ from an uncalcined precursor having a P/Pd molar ratio of 2.09, and the XRD patterns are shown Figure 3.12. The initial reduction at 500 °C produced a mixture of $Pd_3P$ and $Pd_5P_2$ phases,

indicated by the presence of weak $Pd_3P$ peaks at 33.3 and 34.6°. Increasing the reduction temperature and decreasing the $H_2$ flow resulted in the gradual disappearance of these two weak peaks as well as the major overlapped peaks at 40°, and the eventual production of phase pure 5 wt% $Pd_5P_2/SiO_2$. Due to the presence of several overlapped peaks, average particle sizes were not calculated for these catalysts.

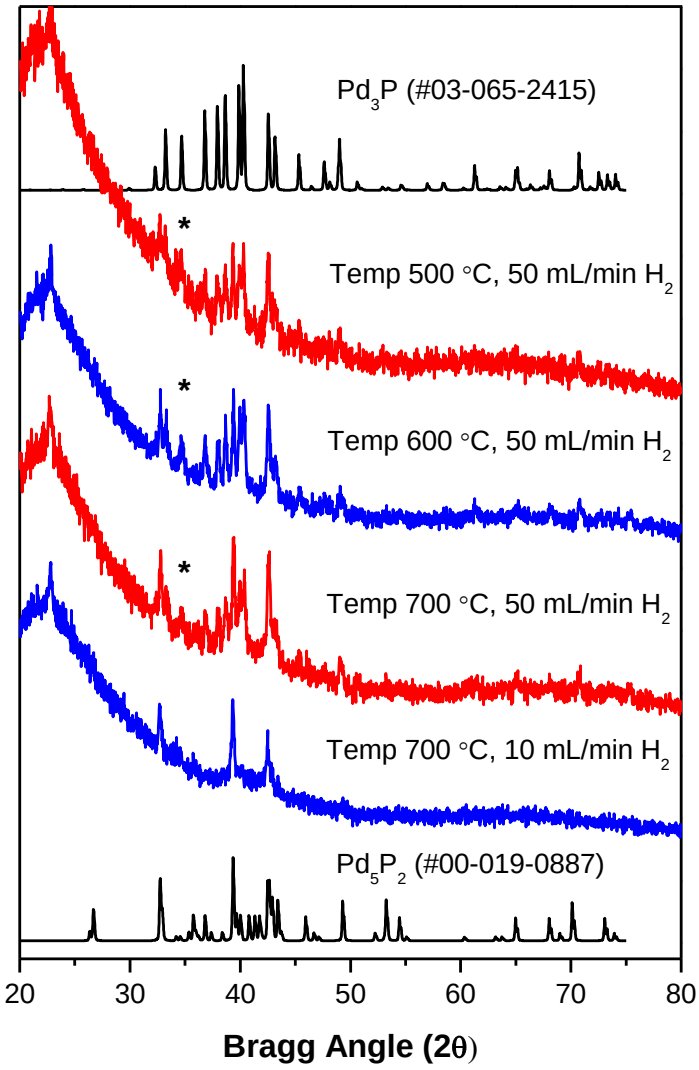


**Figure 3.12 XRD patterns for several 5wt% $Pd_xP_y/SiO_2$ catalysts produced with a P/Pd molar ratio of 2.09.**

An XRD pattern following HDS testing of a 5 wt% $Pd_3P/SiO_2$ catalyst produced from an uncalcined precursor having a P/Pd mole ratio of 0.82 is shown in Figure 3.13. Comparison of the post-HDS pattern with a $Pd_3P$ reference pattern, as well as the as-prepared XRD pattern reveals no loss in catalyst phase purity or average crystallite size.

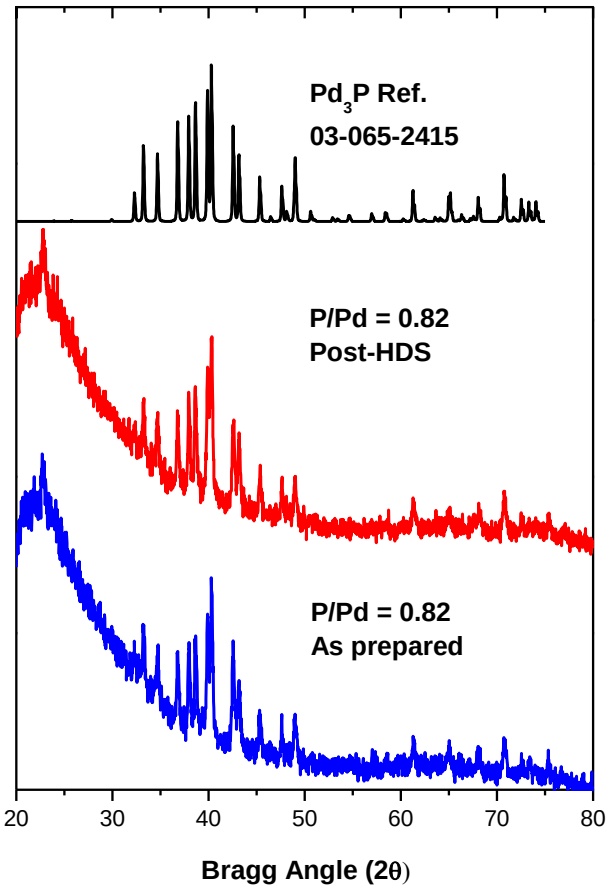


**Figure 3.13 XRD patterns of 5 wt% $Pd_3P/SiO_2$ catalyst, synthesized from an uncalcined precursor using a P/Pd molar ratio of 0.82, before and after DBT HDS testing.**

The post-HDS XRD pattern of a 5 wt% $Pd_5P_2/SiO_2$ catalyst produced from an uncalcined precursor having a P/Pd mole ratio of 2.09 is shown in Figure 3.14.

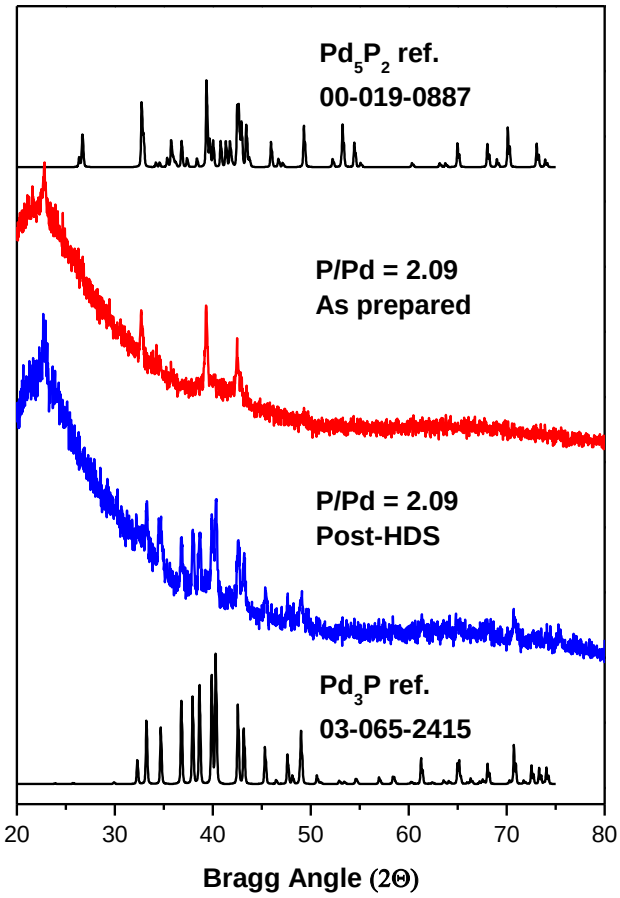


**Figure 3.14 Figure 3.11 XRD pattern of a 5 wt% $Pd_5P_2/SiO_2$ catalyst, synthesized from an uncalcined precursor using a P/Pd molar ratio of 2.09, before and after DBT HDS testing.**

Comparison of the post-HDS pattern with a reference $Pd_5P_2$ pattern, as well as the as-prepared XRD pattern, reveals the 5 wt% $Pd_5P_{2//}SiO_2$ catalyst decomposed under HDS conditions to form $Pd_3P$. The average $Pd_3P$ crystallite size was calculated to be 25 nm using the Scherrer equation and the observed peak at 36.8 °, suggesting no change in average crystallite size.

### 3.1.3 Ruthenium Catalysts

*Supported ruthenium phosphides ($RuP/SiO_2$ and $Ru_2P/SiO_2$)*

The XRD pattern of an as-prepared 15 wt% RuP catalyst synthesized from an uncalcined precursor having a P/Ru molar ratio of 1.11 is shown in Figure 3.15, and indicates phase pure supported RuP was produced. Using the Scherrer equation and the diffraction peak at 31.8°, an average RuP cyrstallite size of 10 nm was calculated.

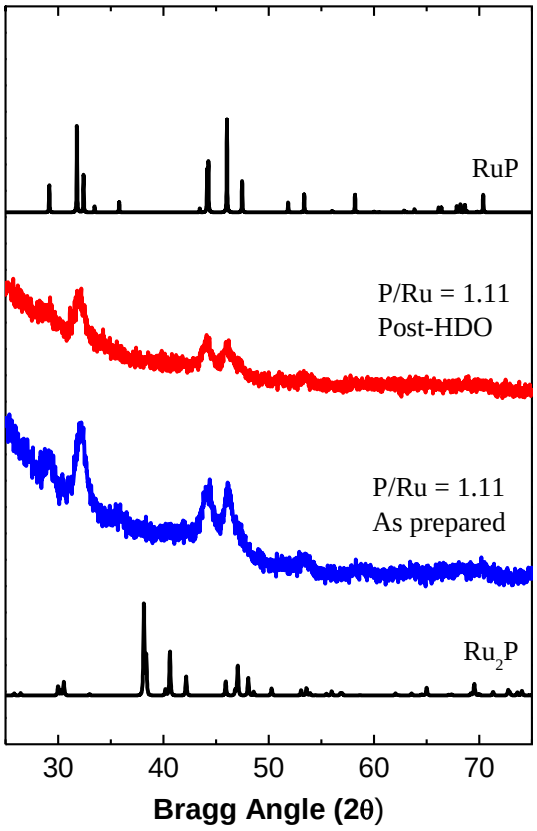


**Figure 3.15 XRD of 15 wt% $RuP/SiO_2$ synthesized with 1.12 P/Ru molar ratio.**

The XRD pattern of the as-prepared 15 wt% $Ru_2P/SiO_2$ catalyst synthesized from an uncalcined precursor with P/Ru=0.86 is shown in Figure 3.16.

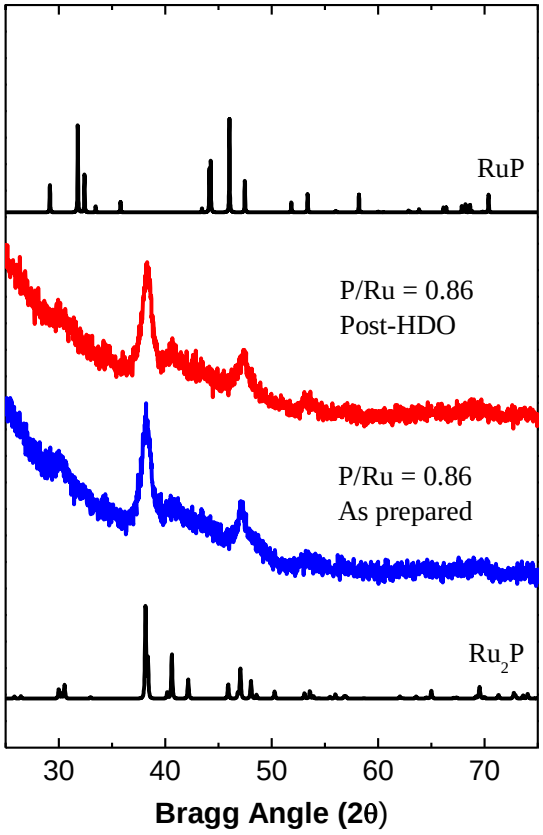


**Figure 3.16 XRD pattern of 15 wt% $Ru_2P/SiO_2$ synthesized with 0.86 P/Ru molar ratio.**

Comparison of the collected pattern with reference patterns indicates phase pure $Ru_2P$ was produced. The average $Ru_2P$ crystallite size was determined to be 10 nm using the Scherrer equation and the diffraction peak at 38.2°.

Additionally, a series of 15 wt% $Ru_xP_y/SiO_2$ catalysts were synthesized with increasing P/Ru mole ratios ($0.60 \leq P/R \leq 1.41$) to explore the effect of precursor composition on catalytic activity. The $Ru_xP_y/SiO_2$ catalysts were characterized by XRD and the patterns are shown in Figure 3.17. A P/Ru mole ratio of 0.60 resulted in a $Ru_2P/SiO_2$

catalyst with some Ru metal impurity present, as indicated by the * symbol above the Ru peak at 44°. P/Ru molar ratios of 0.73 and 0.86 resulted in phase pure $Ru_2P/SiO_2$ catalysts, while P/Ru ratios of 1.0, 1.12, and 1.41 produced phase pure $RuP/SiO_2$ catalysts. Using the Scherrer equation, the average crystallite size for these catalysts was calculated to be ~ 10 nm, indicating that the P/Ru molar ratio had no effect on average crystallite size.

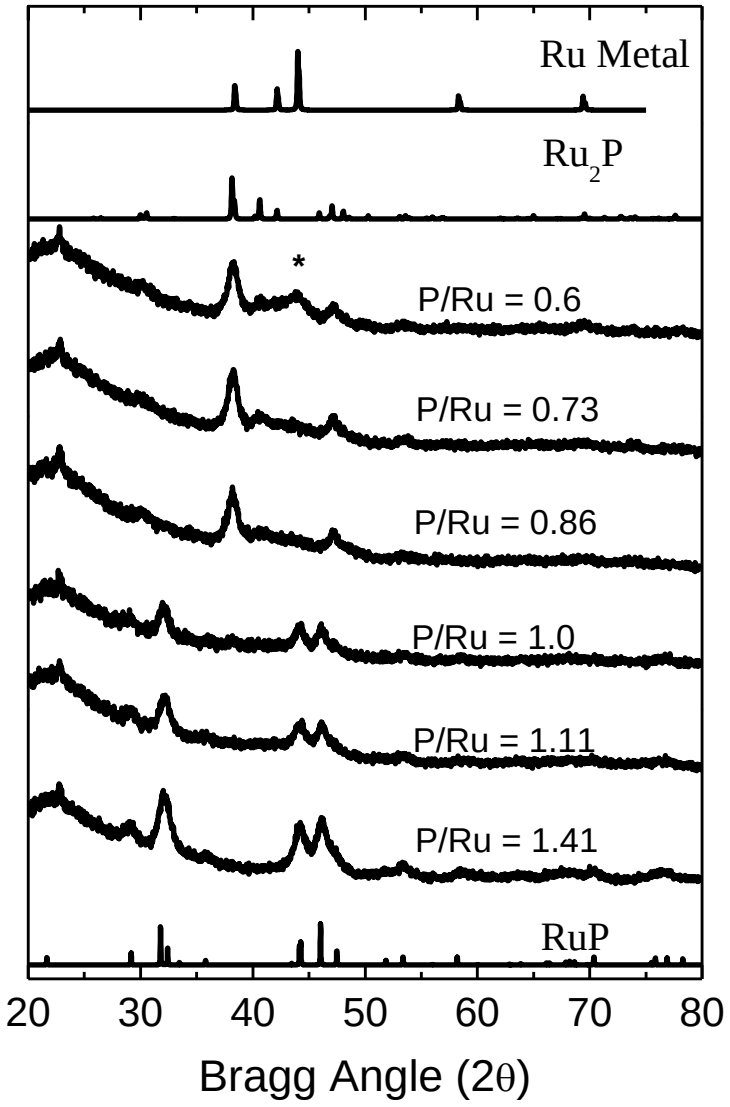


**Figure 3.17 XRD patterns of a series of $Ru_xP_y/SiO_2$ catalysts, synthesized with varying P/Ru molar ratios.**

## 3.2 Transmission Electron Microscopy

Transmission electron microscopy (TEM) images were acquired for selected metal phosphide catalysts to determine average particle sizes and dispersions.

### 3.2.1 Rhodium Catalysts

*Supported rhodium phosphide ($Rh_2P/SiO_2$)*

Low and high resolution TEM images of a 5 wt% $Rh_2P/SiO_2$ catalyst are shown in Figure 3.18. The low-resolution image indicates an even dispersion of $Rh_2P$ particles on the silica phosphide particles on the silica support.

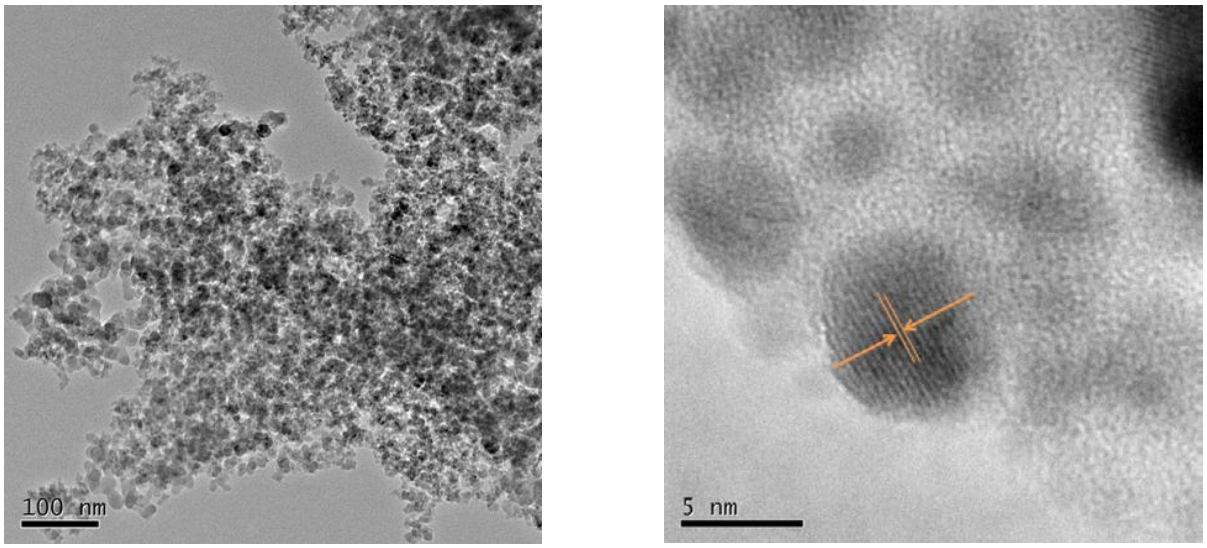


(a) (b)

**Figure 3.18 (a) Low and (b) high resolution TEM images of 5 wt% $Rh_2P/SiO_2$.**

The high resolution image indicates a smaller average particle size than the average crystallite size that was calculated by the Scherrer equation, a discrepancy attributed to the 5 nm detection limit of the XRD technique. Also, the measured spacing of ~ 0.26 nm

between the lattice fringes shown in the high-resolution TEM image corresponds to the reported d-spacing of 0.275 nm for the (200) crystallographic plane of $Rh_2P$.[1]

### *3.2.2 Palladium Catalysts*

*Supported palladium phosphide ($Pd_3P/SiO_2$)*

Low and high-resolution TEM images of a silica supported 5 wt% $Pd_3P/SiO_2$ catalyst, produced from an oxidic precursor and P/Pd mole ratio of 0.79 are shown in Figure 3.19.

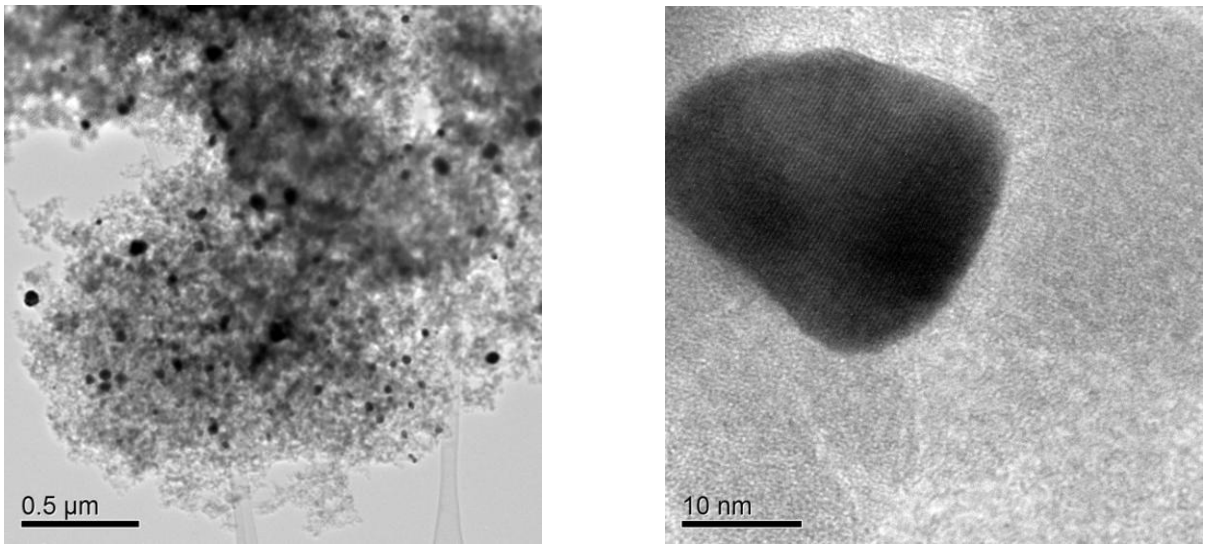


(a) (b)

**Figure 3.19 (a) Low and (b) high resolution TEM images of a 5 wt% $Pd_3P/SiO_2$ catalyst synthesized from a calcined precursor having a P/Pd = 0.79 molar ratio.**

The low resolution image reveals a range of particle sizes while the high resolution image shows a particle with dimensions of 35 nm wide by 25 nm long. Lattice fringes are apparent in the high resolution image of the silica supported $Pd_3P$ particle, indicating its crystalline nature.

### *3.2.3 Ruthenium Catalysts*

*Supported ruthenium phosphides ($RuP/SiO_2$ and $Ru_2P/SiO_2$)*

Low resolution TEM images of 15 wt% $RuP/SiO_2$ and $Ru_2P/SiO_2$ catalysts are shown in figure 3.20.

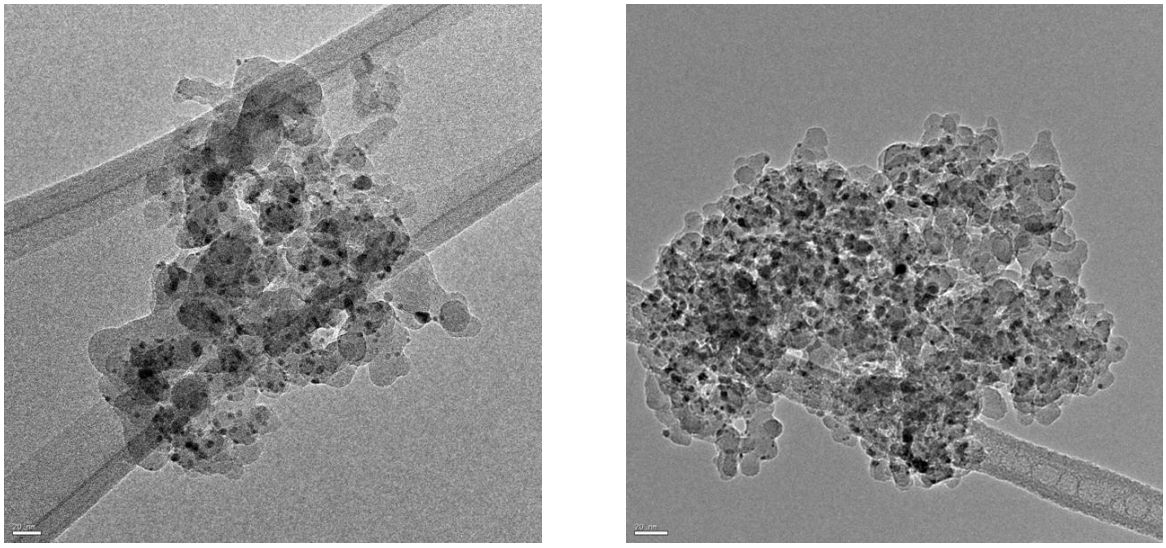

(a) (b)

**Figure 3.20 Low resolution TEM images of (a) a 15 wt% $RuP/SiO_2$ and (b) a 15 wt% $Ru_2P/SiO_2$ catalyst.**

Both images reveal well dispersed ruthenium phosphide particles on the silica support, with average particle sizes of 4 ± 2 nm. The smaller particle sizes determined by TEM images relative to average crystallite sizes calculated from the XRD patterns using the Scherrer equation are likely due to the fact that the smallest ruthenium phosphide crystallites (≤ 5 nm) are below the detection limit for XRD.

## 3.3 X-ray photoelectron spectroscopy

### 3.3.1 Rhodium Catalysts

*Supported rhodium phosphide ($Rh_2P/SiO_2$)*

As-prepared and HDS tested samples of a 5 wt% $Rh_2P/SiO_2$ catalyst were examined using XPS and the resulting spectra are shown in Figure 3.3.1.1.

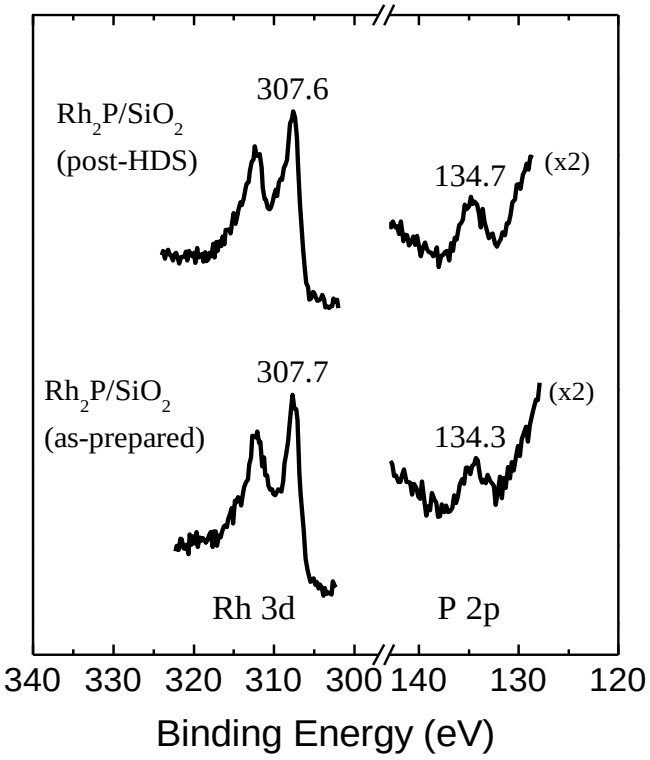


**Figure 3.21 XPS spectra of 5 wt% $Rh_2P/SiO_2$ as-prepared and HDS-tested.**

The spectra in the Rh $3d_{5/2}$ region show a peak at 307.7 eV for the as-prepared catalyst and 307.6 eV for the HDS-tested catalyst. These peaks are above the reported binding energy range of rhodium metal (307.0-307.4 eV) but well below the reported binding energy for $Rh^{3+}$ in $Rh_2O_3$ (308.5 eV),[2] indicating the Rh in $Rh_2P$ bears a partial positive charge ($Rh^{\delta+}$) due to a small donation of electron density to phosphorous. The observed peaks in the P $2p_{3/2}$

region have a binding energy of 134.3 eV for the as-prepared catalyst and 134.7 eV for the HDS tested catalyst and are in the range reported for the $P^{5+}$ species in $Ni_3(PO_4)_2$ (133.3 eV).[2] These peaks can be attributed to the passivation layer formed around the phosphide particles resulting from exposure of the catalysts to a 1 mol% $O_2$/He flow following both synthesis and HDS testing. Analysis of the XPS data results in a surface composition of $Rh_{1.94}P_{1.00}$ and is close to the expected bulk composition of $Rh_2P$.

### *3.3.2 Palladium Catalysts*

*Supported palladium phosphides ($Pd_3P/SiO_2$) – calcined precursors*

An XPS spectrum of a 5 wt% $Pd_3P/SiO_2$ catalyst synthesized from a calcined precursor using a P/Pd molar ratio of 0.79 is shown in Figure 3.22. The spectrum for the Pd $3d_{5/2}$ region indicates a binding energy of 335.2 eV, which falls in the range of the reported binding energy of 334.1-335.8 eV for Pd metal, indicating $Pd^0$ species are present in the $Pd_3P$.[2] Similar to the $Rh_2P$ catalysts, a binding energy of 134.7 eV was obtained in the P 2p region, indicating the $P^{5+}$ species associated with the passivation layer.

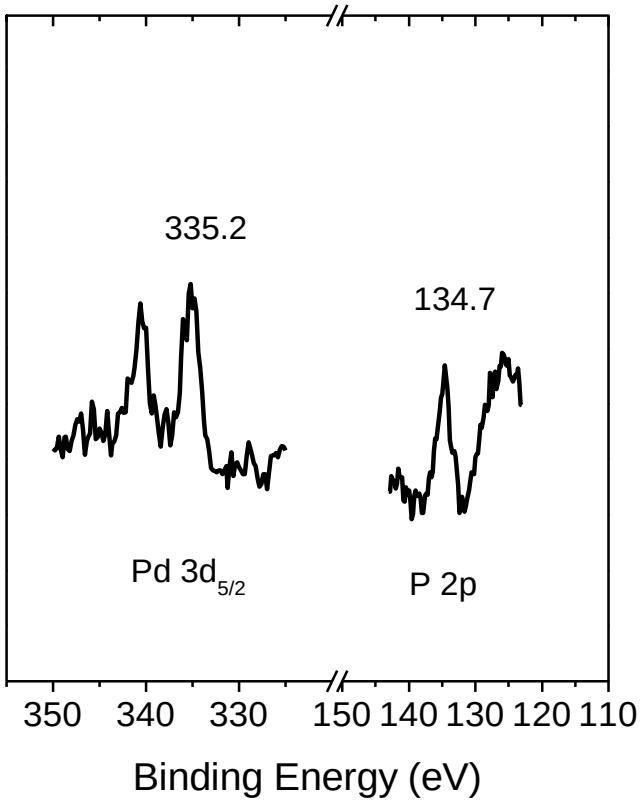


**Figure 3.22 XPS spectra of a 5 wt% $Pd_3P/SiO_2$ catalyst prepared from a calcined precursor having a P/Pd = 0.79 mole ratio.**

## 3.4 BET surface area and chemisorption capacities

### *3.4.1 Rhodium Catalysts*

The BET surface areas and chemisorption capacities for the rhodium metal catalyst ($Rh/SiO_2$) and rhodium phosphide catalyst ($Rh_2P/SiO_2$) are listed in table 3.4.1. Both the rhodium metal and rhodium phosphide catalysts had similar chemisorption capacities following the standard reduction pretreatment. However, the 5 wt% $Rh_2P/SiO_2$ catalyst had almost twice the chemisorption capacity of the 4.4 wt% $Ru/SiO_2$ catalyst following the sequential pretreatment in $H_2$ and then $H_2S/H_2$. BET surface areas were higher for the $Rh/SiO_2$ catalysts than for the $Rh_2P/SiO_2$ catalyst, similar to the trend reported by Gaudette.[3]

**Table 3.1 BET surface areas and chemisorption capacities for rhodium catalysts.**

| Catalyst | BET Surface Area (m2/g) | Chemisorption Capacity (μmol CO/g) | | |
|---|---|---|---|---|
| | | $H_2$ pretreatment | $H_2$ + $H_2S/H_2$ pretreatment | $H2S/H_2$ pretreatment |
| $Rh_2P/SiO_2$ | 128 | 68 | 41 | ----- |
| $Rh/SiO_2$ | 142 | 72 | 22 | ----- |
| Sulf. $Rh/SiO_2$ | 139 | ----- | ----- | 18 |

### *3.4.2 Palladium Catalysts*

The BET surface areas and chemisorption capacities for palladium and palladium phosphide catalysts produced from calcined precursors are shown in Table 3.2.

**Table 3.2 BET surface areas and chemisorption capacities for calcined Pd catalysts.**

| Catalyst | BET surface area | Chemisorption capacity |
|---|---|---|
| | ($m^2$/g) | (μmol CO/g) |
| $Pd/SiO_2$ | 121 | 7.0 |
| Sulf. $Pd/SiO_2$ | 103 | 1.0 |
| $Pd_3P/SiO_2$ | 115 | 9.2 |
| $Pd_5P_2/SiO_2$ | 83 | 12.1 |

The BET surface areas and chemisorption capacities for palladium and palladium phosphide catalysts produced from uncalcined $PdCl_2/SiO_2$ precursors are shown in Table 3.3.

**Table 3.3 BET surface areas and chemisorption capacities for uncalcined Pd catalysts.**

| Catalyst | BET surface area | Chemisorption capacity |
|---|---|---|
| | ($m^2$/g) | (μmol CO/g) |
| $Pd/SiO_2$ | 130 | 30.2 |
| Sulf. $Pd/SiO_2$ | 121 | 7.7 |
| $Pd_3P/SiO_2$ | 133 | 3.7 |
| $Pd_5P_2/SiO_2$ | 96 | 3.2 |

The 4.4 wt% $Pd/SiO_2$ catalyst prepared from the uncalcined precursor had the highest chemisorption capacity of the palladium catalysts, having a CO capacity four times higher than the sulfided $Pd/SiO_2$ catalyst and almost ten times higher than the palladium phosphide catalysts.

### *3.4.3 Ruthenium Catalysts*

BET surface area and chemisorption capacities for the ruthenium and ruthenium phosphide catalysts are shown in Table 3.3.

**Table 3.4 BET surface areas and chemisorption capacities for uncalcined Ru catalysts.**

| Catalyst | BET surface area | Chemisorption capacity |
|---|---|---|
| | ($m^2$/g) | (μmol CO/g) |
| $Ru_2P/SiO_2$ | 150 | 110 |
| $RuP/SiO_2$ | 142 | 92 |
| $Ru/SiO_2$ | 160 | 72 |

While the BET surface areas are similar for the catalysts, the chemisorption capacities differ substantially. The $Ru_2P/SiO_2$ catalyst had the highest CO chemisorption capacity, followed by the $RuP/SiO_2$ catalyst, while the reduced ruthenium metal ($Ru/SiO_2$) catalyst had lowest CO chemisorption capacity of the series.

## 3.5 Sulfur Analysis

### *3.5.1 Rhodium Catalysts*

Figure 3.23 shows the results of sulfur content analyses for 5 wt% $Rh_2P/SiO_2$ and 4.4 wt% $Rh/SiO_2$ catalysts subjected to a $H_2$ then $H_2/H_2S$ pretreatment.

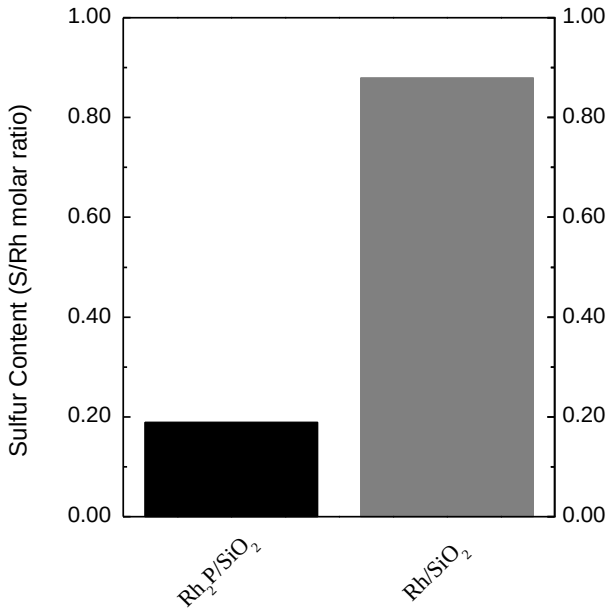


**Figure 3.23 Sulfur content for 5 wt% $Rh_2P/SiO_2$ and 4.4 wt% $Rh/SiO_2$ catalysts following $H_2S/H_2$ treatment.**

The 4.4 wt% $Rh/SiO_2$ catalyst (Rh/S = 0.88) had a sulfur content approximately 4.5 times higher than the 5 wt% $Rh_2P/SiO_2$ catalyst (Rh/S = 0.19), indicating substantial site blockage due to irreversibly bonded S.

### *3.5.2 Palladium Catalysts*

Sulfur incorporation data are shown in Figure 3.24 for a series of 5 wt% palladium catalysts, following DBT HDS activity measurements.

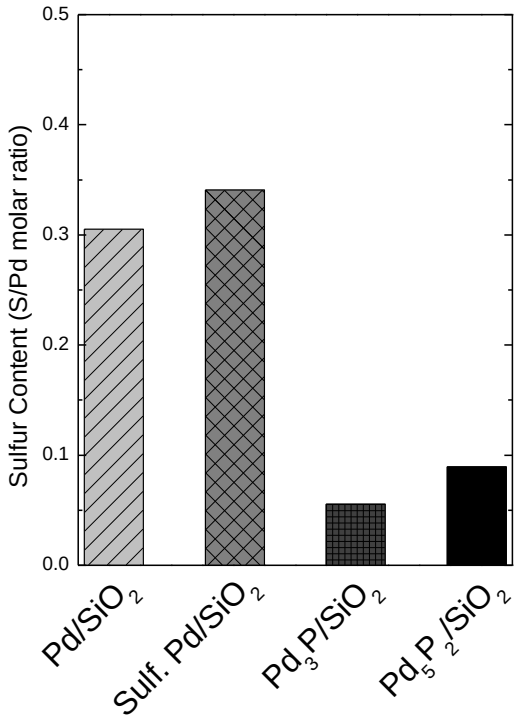


**Figure 3.24 Sulfur content following HDS testing for 4.4 wt% $Pd/SiO_2$, sulfided 4.4 wt% $Pd/SiO_2$, 5 wt% $Pd_3P/SiO_2$, and 5 wt% $Pd_5P_2/SiO_2$ catalysts prepared from uncalcined precursors.**

Both the reduced $Pd/SiO_2$ (S/Pd = 0.31) and sulfided $Pd/SiO_2$ (S/Pd = 0.34) catalysts had almost four times as much sulfur as the $Pd_5P_2/SiO_2$ catalyst (S/Pd molar ratio = 0.08) and 6 times the sulfur content as the $Pd_3P/SiO_2$ catalyst (S/Pd = 0.055). The results indicate that the palladium phosphide catalysts are more resistant to site blockage due to sulfur poisoning.

## 3.6 Hydrodesulfurization

### *3.6.1 Rhodium Catalysts*

Dibenzothiophene hydrodesulfurization (HDS) activity measurements were carried out for the 5 wt% $Rh_2P/SiO_2$ catalyst as a function reaction temperature, time on stream, and partial pressure of $H_2S$. For comparison purposes, 5 wt% $Rh/SiO_2$ and sulfided 5 wt% $Rh/SiO_2$ catalysts, as well as a commercial sulfided Co-$Mo/Al_2O_3$ catalyst were also tested. The DBT conversion as a function of temperature for the catalysts is shown in Fig. 3.25.

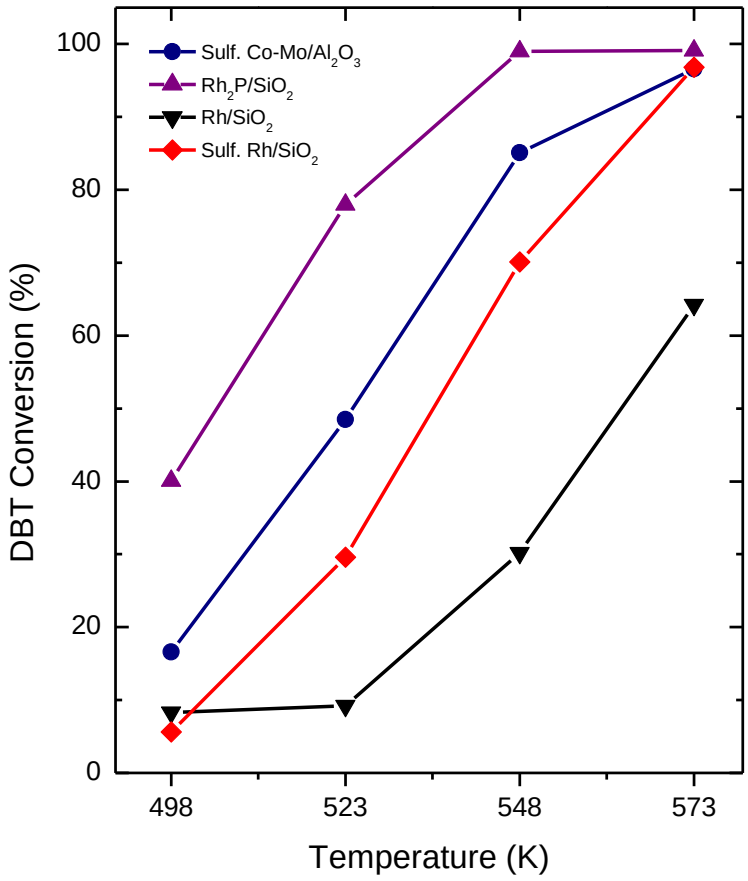


**Figure 3.25 DBT conversion vs. reaction temperature for 4.4 wt% $Rh/SiO_2$, sulfided 4.4 wt% $Rh/SiO_2$, 5wt% $Rh_2P/SiO_2$, and sulfided Co-$Mo/Al_2O_3$ catalysts.**

For the temperatures tested, the reduced 5 wt% $Rh_2P/SiO_2$ catalyst exhibited the highest DBT conversion, achieving nearly 100% DBT conversion by 548 K, while the industrial Co-Mo-$Al_2O_3$ catalyst converted almost 85% and the sulfided 5 wt% $Rh/SiO_2$ catalyst converted 65% at 548 K. The reduced 5 wt% $Rh/SiO_2$ converted the least amount of DBT at 548 K, achieving only 30% conversion. The 5 wt% $Rh_2P/SiO_2$ and sulf. 5 wt% $Rh/SiO_2$ catalysts also exhibited a high selectivity for hydrogenated products, producing almost exclusively bicyclohexane (BCH) and cyclohexylbenzene (CHB) at 548 K, as shown in Figure 3.26. The reduced 5 wt% $Rh/SiO_2$ catalyst also favored the hydrogenated products, while the commercial sulfided Co-Mo/$Al_2O_3$ catalyst favored the direct desulfurization pathway, producing mostly biphenyl (BP).

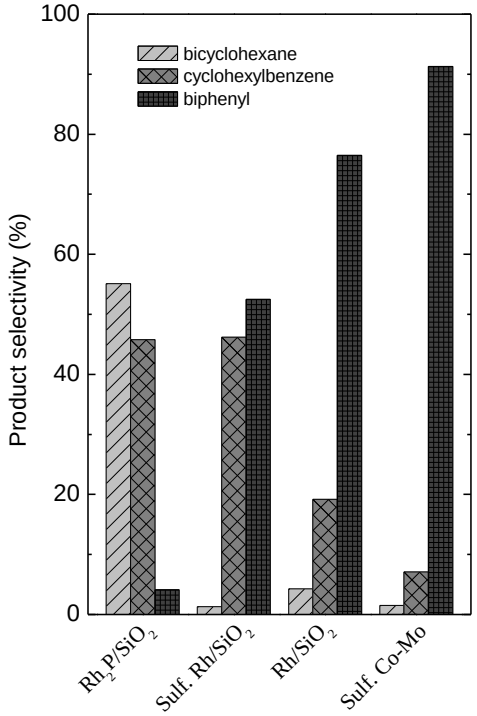


**Figure 3.26 DBT HDS product distributions at 548 K for 4.4 wt% $Rh/SiO_2$, sulfided 4.4 wt% $Rh/SiO_2$, 5wt% $Rh_2P/SiO_2$, and sulfided Co-Mo/$Al_2O_3$ catalysts.**

To assess the stability of the 5 wt% $Rh_2P/SiO_2$ catalyst, two experiments were conducted. First, the 5 wt% $Rh_2P/SiO_2$ was tested for DBT HDS activity at 573 K over the course of 100 h. As shown in Figure 3.27, the DBT HDS activity of the 5 wt% $Rh_2P/SiO_2$ remained

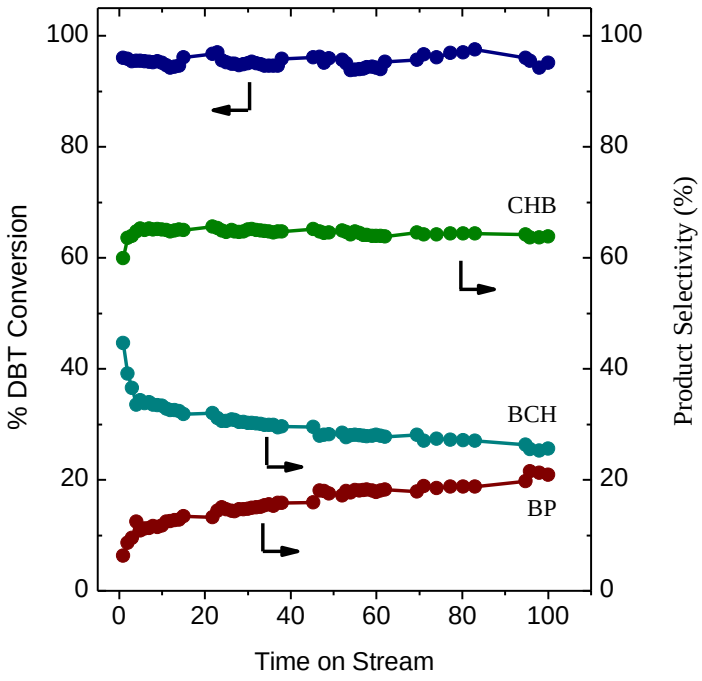


**Figure 3.27 DBT conversion and product selectivity at 573 K vs. time for a 5wt% $Rh_2P/SiO_2$ catalyst.**

steady at 94-99% conversion, with no indication of deactivation over time. The product distribution did change, however, with the production of biphenyl (BP) increasing over time at the expense of bicyclohexane (BCH) production. The selectivity towards cyclohexylbezene (CHB) remained relatively constant at 54-59% over the course of the experiment. In the second experiment, the DBT HDS conversions for both 5 wt% $Rh_2P/SiO_2$ and 4.4 wt% $Rh/SiO_2$ were measured while co-feeding increasing amounts of $H_2S$ (0-50 kPa) with the 3000 ppm DBT/decalin reactor feed. After the final 50 kPa $H_2S$ co-feed

measurement was conducted, the $H_2S$ co-feed was stopped and the recovered HDS activity was measured. The results are shown in Figure 3.28.

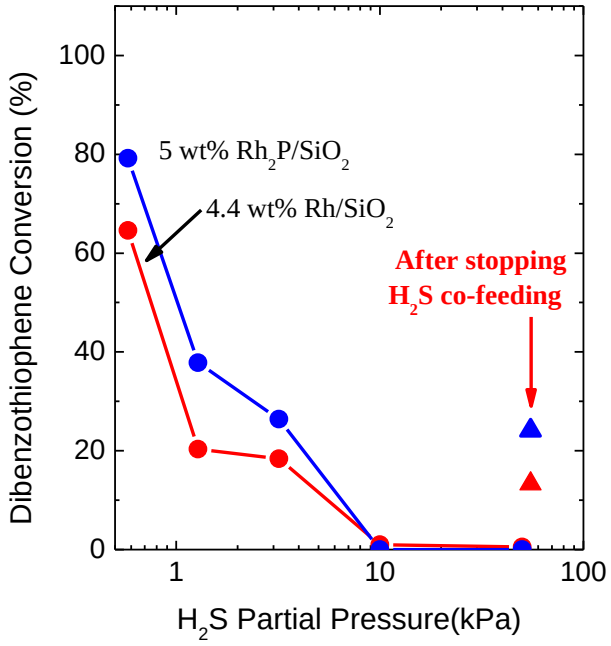


**Figure 3.28 DBT HDS activity at 573 K vs. $H_2S$ partial pressure.**

Upon start of $H_2S$ co-feeding (1 kPa $H_2S$), the activity of both catalysts dropped dramatically, with the 5 wt% $Rh_2P/SiO_2$ catalyst activity dropping by 50% and the 4.4 wt% $Rh/SiO_2$ activity decreasing by 66%. Catalyst activity decreased further with the addition of increasing amounts of $H_2S$, with no activity measured when 10 kPa of $H_2S$ or higher pressures were co-fed. Once the $H_2S$ co-feeding was stopped (after 50 kPa $H_2S$), the DBT HDS activity rebounded to 24% DBT conversion of the 5 wt% $Rh_2P/SiO_2$ catalyst and 13% DBT conversion for the 4.4 wt% $Rh_2P/SiO_2$ catalyst.

### *3.6.2 Palladium Catalysts*

*Supported palladium phosphide ($Pd_3P/SiO_2$) – calcined precursor*

DBT HDS activity measurements were carried out for a 5 wt% $Pd_3P/SiO_2$ catalyst prepared from a calcined $Pd/SiO_2$ precursor having a P/Pd mole ratio of 0.79. For comparison purposes, the reduced and sulfided 4.4 wt% $Pd/SiO_2$ catalysts were also tested. As shown in Figure 3.29, the 5 wt% $Pd_3P/SiO_2$ had the highest DBT HDS activity at 548 K. The HDS activity continued to increase with temperature, but peaked at 623 K.

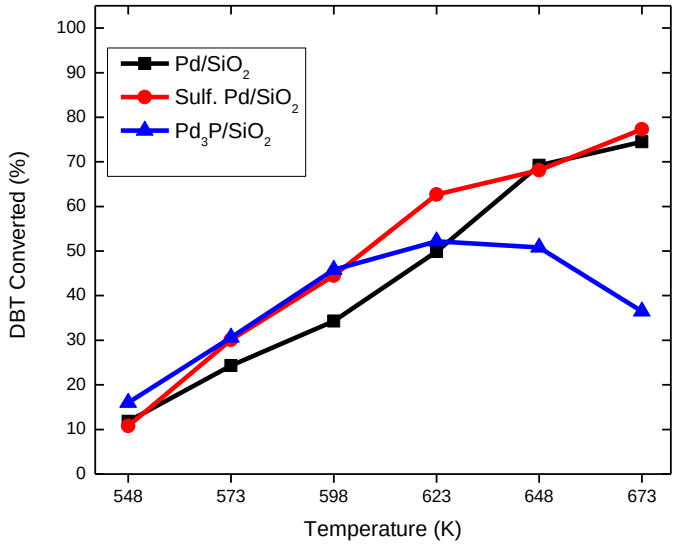


**Figure 3.29 DBT HDS conversion vs. temperature for 4.4 wt% $Pd/SiO_2$, sulfided 4.4 wt% $Pd/SiO_2$, and 5 wt% $Pd_3P/SiO_2$ catalysts synthesized from calcined precursors.**

At temperatures above 623 K, the DBT HDS activity of the 5 wt% $Pd_3P$ decreased with increased temperature. The DBT HDS activity for the 4.4 wt% $Pd/SiO_2$ catalyst was higher than the DBT HDS activity of the sulfided 4.4 wt% $Pd/SiO_2$ catalyst up to 623 K. At

temperatures above 623 K, DBT HDS activity was similar for the $Pd/SiO_2$ and the sulfided $Pd/SiO_2$ catalysts.

The HDS product selectivities at 623 K for the 4.4 wt% $Pd/SiO_2$, sulfided 4.4 wt% $Pd/SiO_2$, and 5 wt% $Pd_3P/SiO_2$ catalysts are shown in Figure 3.30. The sulfided 4.4 wt% $Pd/SiO_2$ catalyst exhibited the highest selectivity towards hydrogenated (HYD) products, followed by the reduced 4.4 wt% $Pd/SiO_2$ catalyst. While the 5 wt% $Pd_3P/SiO_2$ favored hydrogenated products, the product selectivity was not as biased towards hydrogenated products as for the two $Pd/SiO_2$ catalysts.

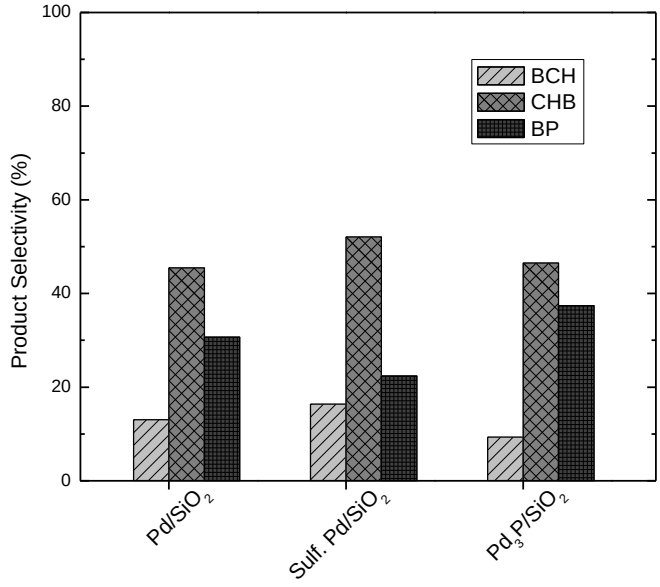


**Figure 3.30 DBT HDS product selectivities at 623 K for 4.4 wt% $Pd/SiO_2$, sulfided 4.4 wt% $Pd/SiO_2$, and 5 wt% $Pd_3P/SiO_2$ catalysts synthesized from calcined precursors.**

*Supported palladium phosphides ($Pd_3P/SiO_2$ and $Pd_5P_2/SiO_2$) – uncalcined precursor*

Silica supported palladium phosphide catalysts (5 wt% $Pd_3P/SiO_2$ and $Pd_5P_2$), prepared from uncalcined $PdCl_2/SiO_2$ precursors, were also tested for DBT HDS activity and the results are shown in Figure 3.31.

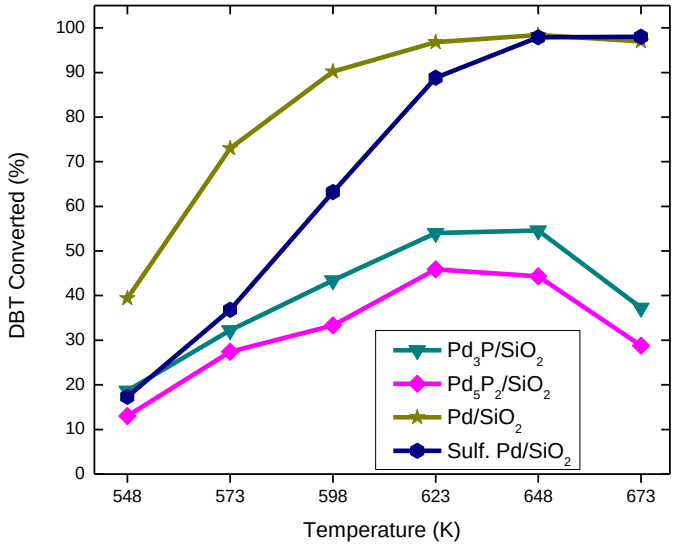


**Figure 3.31 DBT HDS conversion vs. temperature for 4.4 wt% $Pd/SiO_2$, sulfided 4.4 wt% $Pd/SiO_2$, 5 wt% $Pd_3P/SiO_2$, and 5 wt% $Pd_5P_2/SiO_2$ catalysts synthesized from uncalcined precursors.**

At 548 and 573 K, the DBT conversion for the reduced $Pd/SiO_2$ catalyst was more than twice the DBT activity of the other catalysts tested, with the reduced $Pd/SiO_2$ catalyst converting 40% of the DBT at 548 K and 72% at 573 K, before achieving 100% conversion by 623 K. DBT activity for the sulfided $Pd/SiO_2$ catalyst started much lower, converting only 17% and 37% of the DBT at 548 and 573 K, respectively. 100% DBT conversion for the sulfided catalyst was achieved by 648 K. Similar to the palladium phosphide catalysts (calcined precursors) previously tested, the $Pd_3P/SiO_2$ and $Pd_5P_2/SiO_2$ catalysts (uncalcined precursors) were less active than the $Pd/SiO_2$ catalysts. The $Pd_3P/SiO_2$ catalyst was slightly more active than the sulfided $Pd/SiO_2$ at 548 K, converting almost 18% of the DBT, but only converted 32% at 573 K. DBT activity for the $Pd_3P/SiO_2$ peaked at 623 K, converting 55% of the DBT. As observed for the palladium phosphide catalysts prepared from calcined precursors, DBT activity fell for the $Pd_3P/SiO_2$ and $Pd_5P_2/SiO_2$ (uncalcined precursors) catalysts at 648-673 K, with the

$Pd_3P/SiO_2$ catalyst converting 37% of the DBT and the $Pd_5P_2/SiO_2$ converting 28% of the DBT at 673 K. The $Pd_5P_2/SiO_2$ catalyst was the least active at all temperatures, paralleling the activity trends observed for the $Pd_3P/SiO_2$ catalyst, except at lower DBT conversion.

The HDS product selectivities at 623 K for the 4.4 wt% $Pd/SiO_2$ and sulfided $Pd/SiO_2$ catalysts, as well as the 5 wt% $Pd_3P/SiO_2$ and $Pd_5P_2/SiO_2$ catalysts are shown in Figure 3.32.

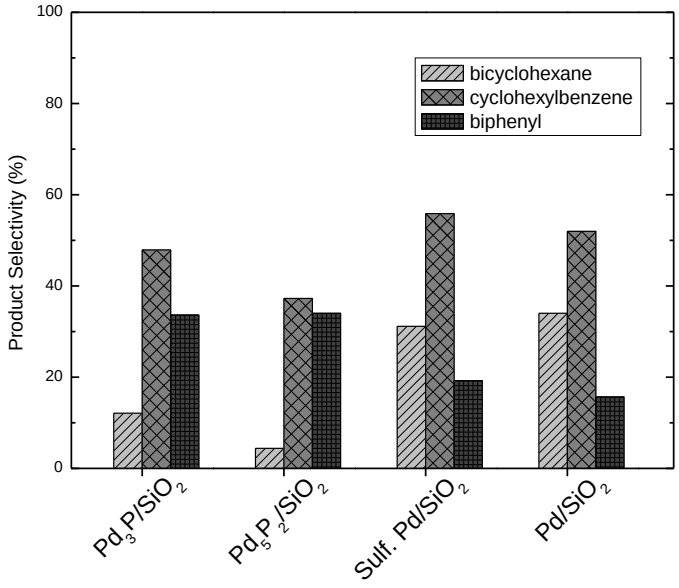


**Figure 3.32 Product distributions at 623 K for 4.4 wt% $Pd/SiO_2$, sulfided 4.4 wt% $Pd/SiO_2$, 5 wt% $Pd_3P/SiO_2$, and 5 wt% $Pd_5P_2/SiO_2$ catalysts synthesized from uncalcined precursors.**

Similar to the product selectivities observed for the palladium catalysts synthesized from calcined precursors, the 4.4 wt% $Pd/SiO_2$ and sulfided $Pd/SiO_2$ catalysts synthesized from uncalcined precursors exhibited the highest selectivity towards hydrogenated (HYD) products. The 5 wt% $Pd_3P/SiO_2$ and $Pd_5P_2/SiO_2$ catalysts favored hydrogenated (HYD) products, but biphenyl accounted for a larger amount of the DBT HDS products than for the $Pd/SiO_2$ catalysts.

## 3.7 Hydrodeoxygenation

### *3.7.1 Ruthenium Catalysts*

*Supported ruthenium phosphides ($RuP/SiO_2$ and $Ru_2P/SiO_2$)*

To provide an initial assessment of the hydrodeoxygenation (HDO) properties of ruthenium phosphide catalysts, the furan HDO activity of several ruthenium catalysts was measured at 673 K, and shown in Figure 3.33.

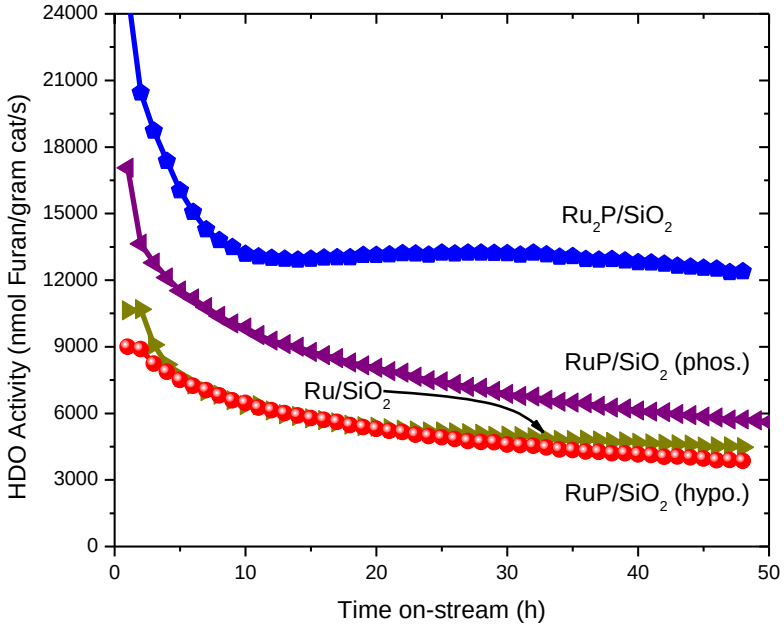


**Figure 3.33 Furan HDO activity at 673 K vs time for 15 wt% $Ru_2P/SiO_2$ 13.5 wt% $RuP/SiO_2$, and 11.9 wt% $Ru/SiO_2$ catalysts.**

While the catalysts tested exhibited an initial decline in activity, the $Ru_2P/SiO_2$ catalyst was the first to stabilize after about 10 h on stream, and the furan HDO activity remained relatively constant for the duration of the testing. The two $RuP/SiO_2$ catalysts showed a similar decline in activity over time, however the $RuP/SiO_2$ catalyst prepared from a

phosphate (phos.) precursor prepared by Pease[3] was nearly 1.5 times as active as the $RuP/SiO_2$ (hypo.) catalyst prepared from the hypophosphite precursor. The $RuP/SiO_2$ (hypo., P/Me=1.1) was the least active, falling below the furan HDO activity of the $Ru/SiO_2$ catalyst after 20 h on stream.

The product distributions for the different catalysts also varied considerably. As shown in Figure 3.34, the 13.5 wt% $Ru_2P/SiO_2$ catalyst favored the production of butane, while the 15 wt% $RuP/SiO_2$ catalyst also favored $C_4H_x$ products, but almost 30% were butenes. The reduced 11.9 wt% $Ru/SiO_2$, however, greatly favored $C_3H_x$ products, a result indicating an undesirable C-C bond cleavage.

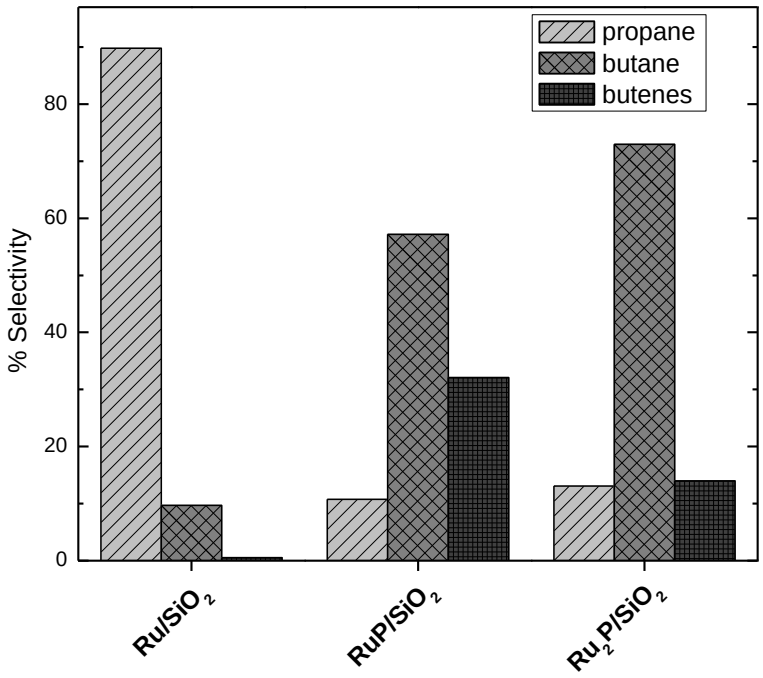


**Figure 3.34 HDO product selectivities for 11.9 wt% $Ru/SiO_2$, 15 wt% $RuP/SiO_2$, and 13.5 wt% $Ru_2P/SiO_2$ catalysts.**

Additional ruthenium phosphide ($Ru_xP_y/SiO_2$) catalysts were also synthesized and tested. Initially, different P/Ru molar ratios were investigated in an attempt to optimize the $Ru_xP_y$ particle size and phase purity. These catalysts were also tested for furan HDO activity. Interestingly, catalyst activity was found to vary not only between different ruthenium phosphide phases ($Ru_2P$ vs RuP) but also for a single phase (e.g. $Ru_2P$) produced from different P/Ru molar ratios, as shown in Figure 3.35.

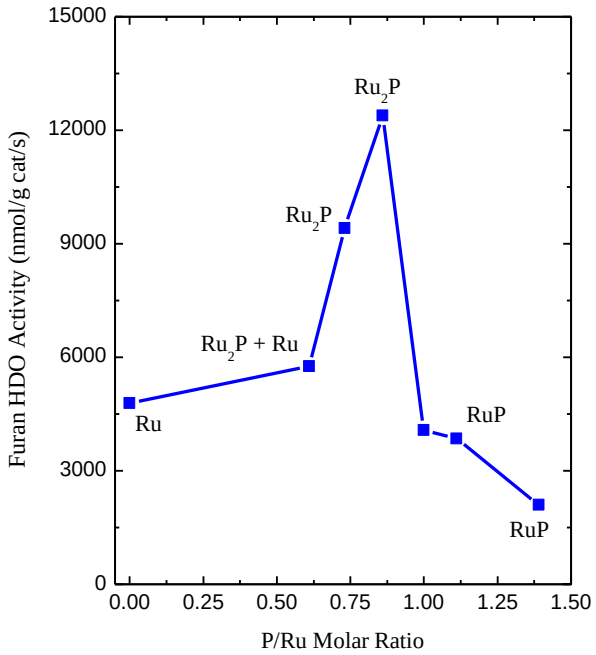


**Figure 3.35 Furan HDO activity at 48 h vs P/Ru molar ratio in the catalyst precursor.**

The 15 wt% $Ru_2P/SiO_2$ prepared from a precursor having a P/Ru molar ratio of 0.86 had the highest overall furan conversion and a 30% higher conversion than the $Ru_2P/SiO_2$ catalyst prepared from a precursor having a P/Ru molar ratio of 0.73. Additionally the 13.5 wt% $RuP/SiO_2$, catalyst (P/Ru=1.12) had almost twice the furan conversion as a similar $RuP/SiO_2$ catalyst prepared from a precursor having a higher molar ratio (P/Ru=1.41).

## References:

1. JCPDS--International Centre for Diffraction Data., PDF-4/full file relational database. International Centre for Diffraction Data: Newtown Square, Pa., 2002.

2. Wagner, C. D., *The NIST X-ray photoelectron spectroscopy (XPS) database*. U.S. Dept. of Commerce, National Institute of Standards and Technology: Gaithersburg, MD :, 1991.

3. Pease, M.L. Novel Ru-Based Hydrodesulfurization Catalysts. Honors Thesis, Western Washington University, Bellingham, 2004.

## Chapter 4. Discussion

As world crude oil reserves continue to be exhausted, unconventional petroleum resources and alternative renewable fuel processes are being developed to meet the increasing demand for transportation fuel. A major problem with many of these resources is the unrefined oil is heavily contaminated: Oil derived from shale and tar sands contains a large amount of high boiling point organosulfur compounds while bio-oils produced from the fast pyrolysis of biomass materials contain large amounts of oxygenated hydrocarbons. These contaminants are undesirable in transportation fuels because their concentration is regulated for environmental reasons, or their presence results in a less stable and more corrosive fuel product. The goal of this research is to develop new catalysts which are more effective at removing these impurities from fuel feedstocks. Several noble metal phosphide catalysts were synthesized and tested for DBT HDS and furan HDO activity to evaluate their potential as hydrotreating catalysts capable of processing these alternative feedstocks.

*Supported rhodium phosphide ($Rh_2P/SiO_2$)*

As confirmed by XRD, silica-supported $Rh_2P$ was prepared by TPR of a calcined precursor impregnated with an aqueous solution of rhodium chloride and ammonium dihydrogen phosphate. The average $Rh_2P$ crystallite size was calculated to be ~10 nm using the Scherrer equation, while a smaller average particle size of 4 nm determined by TEM confirmed that highly dispersed $Rh_2P$ particles were prepared despite a high TPR temperature (923 K). The XPS-measured surface composition for the as-prepared 5 wt% $Rh_2P/SiO_2$ was calculated to be $Rh_{1.94}P_{1.00}$, which is very close to the expected bulk $Rh_2P$ composition. In addition, XPS data in the Rh $3d_{5/2}$ region reveal a binding energy of 307.8

eV, which indicates the Rh of the $Rh_2P/SiO_2$ catalyst bears a partial positive charge ($Rh^{\delta+}$). However, determination of the oxidation state of Rh is complicated by the presence of the outer passivation layer surrounding the $Rh_2P$ particles, necessary to prevent deep oxidation of the prepared $Rh_2P$ particles following TPR synthesis. The fact that the $3d_{5/2}$ binding energy is just above that for Rh metal is likely due to oxidized Rh species present in this layer, as $^{31}P$ NMR spectral data of silica-supported $Rh_2P$ catalysts reported by Hayes et al.[1] indicate the $Rh_2P$ particles are metallic.

The 5 wt% $Rh_2P/SiO_2$ and the $Rh/SiO_2$ catalysts subjected to the $H_2$ pretreatment had similar CO chemisorption capacities (68 and 72 μmol CO/g catalyst, respectively), suggesting similar active site densities for the two catalysts. However, pretreatment of these catalysts with $H_2$ followed by $H_2S/H_2$ resulted in substantially different chemisorption capacities. The $Rh_2P/SiO_2$ catalyst had a CO capacity of 41 μmol CO/g catalyst, while the $Rh/SiO_2$ catalyst had only 22 μmol CO/g catalyst. The results of sulfur content analyses performed on these catalysts following the $H_2S/H_2$ treatment indicate this difference in chemisorption capacities is the result of active site blockage by strongly bonded sulfur species, as the $Rh/SiO_2$ catalyst had over 4.5 times as much sulfur as the $Rh_2P/SiO_2$ catalyst (S/Rh = 0.88 for the $Rh/SiO_2$ vs. S/Rh = 0/0.19 for the $Rh_2P/SiO_2$ catalyst). Burns et al.[2] report a similar trend of increased S tolerance by a metal phosphide catalyst when they compared $Ni_2P/SiO_2$ and $Ni/SiO_2$ catalysts. In their study, testing several different metal loadings and following the same $H_2S/H_2$ pretreatment procedure, the $Ni_2P/SiO_2$ catalysts consistently had a higher CO chemisorption capacity than the $Ni/SiO_2$ catalyst of an equivalent metal loading.

The 5 wt% $Rh_2P/SiO_2$ catalyst exhibited very high DBT HDS activity, achieving a higher DBT conversion than both the $Rh/SiO_2$ and sulfided $Rh/SiO_2$ catalysts of equivalent Rh loading throughout the temperature range 498-573 K. The $Rh_2P/SiO_2$ catalyst also demonstrated excellent stability, maintaining near constant DBT conversion (94-99%) over a 100 h test. XPS and XRD of HDS-tested 5 wt% $Rh_2P/SiO_2$ catalysts indicated no significant changes in phase purity, crystallite size, or chemical composition.

The DBT HDS product selectivity for the 5 wt% $Rh_2P$ catalyst differed substantially from those of the reduced and sulfided $Rh/SiO_2$ catalysts, as can be seen in Figure 3.26. These data are useful as they indicate the pathway by which the catalysts desulfurize DBT. It is widely accepted that the HDS of DBT can be accomplished through two different mechanisms, shown in Figure 4.1.[3,4,5]

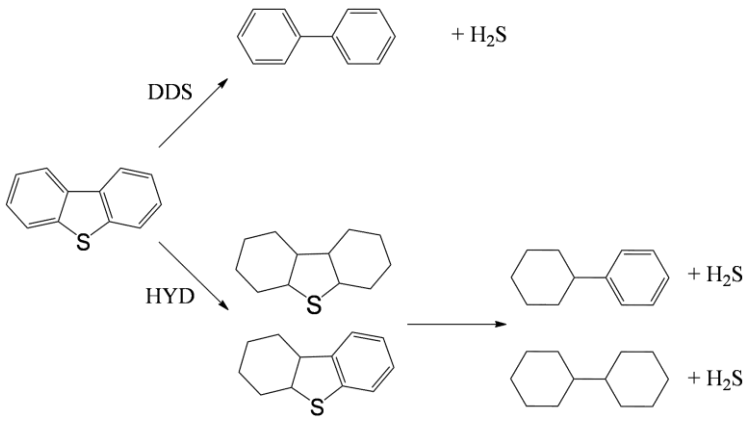


**Figure 4.1 HDS pathways for dibenzothiophene.**

At 548 K, the $Rh_2P/SiO_2$ catalyst strongly favored the HYD pathway (96%), in which one or both of the benzene rings are hydrogenated prior to the removal of the sulfur, whereas the reduced $Rh/SiO_2$ favored the DDS pathway (76%). The sulfided $Rh/SiO_2$ catalyst was almost evenly split between the DDS (52%) and the HYD (48%) pathways for DBT HDS.

The substantial difference in DBT HDS activities observed for the $Rh_2P/SiO_2$ and $Rh/SiO_2$ catalysts can be understood by examining the reaction pathways to catalytically process DBT, and recognizing the corresponding effect the enhanced resistance to sulfur incorporation observed by the $Rh_2P/SiO_2$ catalyst has on this process. While noble metals are well-known hydrogenation catalysts, they are highly susceptible to sulfur poisoning and, therefore, can only be used for HDS processing during which the $H_2S$ partial pressure is kept low. As shown in Figure 4.2, the phenyl rings of the planar DBT molecule sterically hinder adsorption via the sulfur atom onto the catalyst surface, slowing the DDS pathway for DBT HDS.

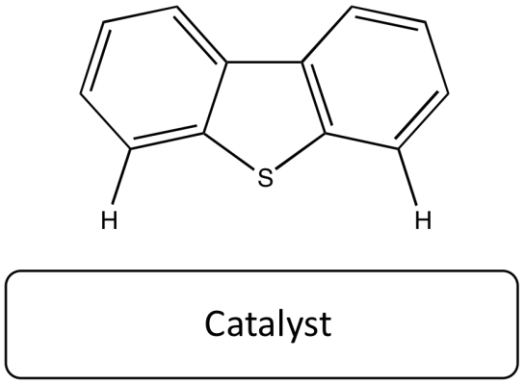


**Figure 4.2 Steric hinderance of the adjacent phenyl rings of DBT.**

Initial hydrogenation of one or both of the benzene rings, as shown by the HYD pathway, breaks the planarity of the DBT molecule and allows adsorption via the sulfur atom to more easily occur on the catalyst. Once the sulfur can bind more readily to the active site, the increased resistance to sulfur incorporation of $Rh_2P/SiO_2$ prevents the sulfur from irreversibly binding in the active site once the C-S bonds are cleaved and, therefore, poisoning the catalyst. This is likely the cause for the much lower DBT HDS activity observed

for the $Rh/SiO_2$ catalysts, as the post-HDS sulfur analysis reveal a much higher S content for the $Rh/SiO_2$ catalyst.

*Supported palladium phosphides ($Pd_3P/SiO_2$ and $Pd_5P_2$)*

XRD analysis confirmed the synthesis of 5 wt% $Pd_3P/SiO_2$ and $Pd_5P_2/SiO_2$ from calcined and uncalcined $PdCl_2/SiO_2$ precursors, impregnated with aqueous ammonium hypophosphite solutions. While similar P/Pd molar ratios and TPR conditions resulted in phase pure $Pd_3P$ from both calcined and uncalcined precursors, different P/Pd metal ratios and TPR conditions were necessary to obtain phase pure $Pd_5P_2/SiO_2$. Using a calcined precursor, a of P/Pd ratio of 3.5 and reduction temperature of 873 K produced phase pure $Pd_5P_2$, whereas using an uncalcined $PdCl_2/SiO_2$ precursor having a P/Pd ratio of 2.09 produced phase pure $Pd_5P_2$ when reduced in a 10 mL/min flow of $H_2$ at 973 K. Using the uncalcined $PdCl_2/SiO_2$ precursor did, however, produce larger average $Pd_5P_2$ crystallite sizes when compared to the phase pure $Pd_5P_2$ catalyst prepared using the calcined precursor. This is likely due to the higher reduction temperatures required when using a lower P/Pd molar ratio.

DBT HDS activity measurements were conducted to compare the HDS properties of $Pd_3P/SiO_2$, $Pd_5P_2/SiO_2$, and $Pd/SiO_2$ catalysts. The 5 wt% $Pd_3P/SiO_2$, $Pd/SiO_2$, and sulfided $Pd/SiO_2$ catalysts, all prepared from a calcined precursor, exhibited similar DBT HDS conversion trends at 548 K to 623 K, with increasing DBT conversion as the temperature was increased. The $Pd_3P/SiO_2$ catalyst was the most active at 548 K, being more than twice as active as the $Pd/SiO_2$ catalysts. The $Pd_3P/SiO_2$ continued to be the most active at 573 and 598 K, but the trend of increasing HDS activity with increasing temperature slowed

dramatically above 598 K. The DBT HDS activity peaked for the $Pd_3P/SiO_2$ catalyst at 623 K and declined with continued increase in temperature, while the HDS activity for the reduced and sulfided $Pd/SiO_2$ catalysts continued to increase as the temperature was increased (623-673 K). The decline in activity for the $Pd_3P/SiO_2$ did not appear to be the result of sulfur poisoning, as post-HDS sulfur analyses revealed a much lower S/Pd molar ratio for the $Pd_3P/SiO_2$ catalyst compared to the reduced and sulfided $Pd/SiO_2$ catalysts. While all three palladium catalysts favored the HYD pathway for DBT HDS activity, surprisingly, the 5 wt% $Pd_3P/SiO_2$ catalyst produced the most biphenyl, accounting for 40% of the products at 623 K. This result was unexpected, as our results for the $Rh_2P/SiO_2$ catalysts showed hydrogenated products to be strongly favored. The selectivity towards almost 40% biphenyl likely accounts for the lower DBT HDS activity observed for the $Pd_3P/SiO_2$ catalyst, as the DDS pathway for DBT HDS is sterically unfavorable, resulting in a lower overall DBT HDS activity.

HDS activity measurements were also conducted using 5 wt% $Pd_3P/SiO_2$ and $Pd_5P_2/SiO_2$ catalysts prepared from uncalcined $PdCl_2/SiO_2$ precursors impregnated with hypophosphite. The HDS properties of these Pd phosphide catalysts were compared with those of reduced and sulfided 4.4 wt% $Pd/SiO_2$ catalysts also prepared from an uncalcined $PdCl_2/SiO_2$ precursor. The 4.4 wt% $Pd/SiO_2$ catalyst had over twice the DBT HDS activity (39% conversion) at 548 K as the sulfided $Pd/SiO_2$ and $Pd_3P/SiO_2$ catalyst (19% and 18%, respectively), and three times as active as the 5 wt% $Pd_5P_2/SiO_2$ catalyst (13%). The reduced $Pd/SiO_2$ catalyst continued to be significantly more active than the sulfided Pd metal and Pd phosphide catalysts at higher temperatures, achieving nearly 100% DBT conversion by 623

K. While, the sulfided $Pd/SiO_2$ had a similar HDS activity to both the Pd phosphide catalysts at 548 K, the activity increased dramatically over the next two temperature increments, achieving 60% at and nearly 100% DBT conversion at 598 and 648 K, respectively. Interestingly, the uncalcined Pd phosphide catalysts ($Pd_3P/SiO_2$ and $Pd_5P_2$) had similar DBT HDS activity versus temperature profiles, with the $Pd_3P/SiO_2$ consistently maintaining a 10% higher conversion than the $Pd_5P_2/SiO_2$ catalyst (See figure 3.31). Similar to the trend observed for the 5 wt% $Pd_3P/SiO_2$ catalyst prepared from a calcined precursor, the $Pd_3P/SiO_2$ and $Pd_5P_2/SiO_2$ catalysts prepared from uncalcined precursors exhibited gradual increase in DBT HDS activity as the temperature was increased (548-623 K); at 623 K the uncalcined 5 wt% $Pd_3P/SiO_2$ catalyst achieved a 50% DBT conversion while the $Pd_5P_2/SiO_2$ catalyst achieved 42% DBT conversion. DBT HDS activity then decreased for both catalysts over the final two temperature increments. Post-HDS XRD patterns help to understand the similarity in activity between the silica-supported $Pd_3P$ and $Pd_5P_2$ phases as the post-HDS XRD pattern of the $Pd_5P_2/SiO_2$ catalyst revealed that $Pd_5P_2$ converted to $Pd_3P$ during the HDS activity measurement. It is possible that the excess phosphorous needed in the synthesis of the $Pd_5P_2$ catalyst (P/Pd = 2.09) and/or from the subsequent decomposition of the $Pd_5P_2$ remained on the surface of the Pd phosphide particles, poisoning active sites.

Palladium phosphides catalysts do exhibit several promising trends suggesting potential as deep-HDS catalysts. Sulfur analyses of palladium and palladium phosphide catalysts following HDS testing and shown in Figure 3.24, reveal palladium phosphides have an increased resistance to sulfur incorporation, in comparison to palladium and palladium sulfide (sulf. palladium) catalysts. And while chemisorption data indicate low active site

density for the palladium phosphides prepared in this research, DBT HDS activity per active site, or turnover frequency (TOFs), for palladium phosphides is much higher than those for palladium catalysts or rhodium phosphide (Figure 4.3).

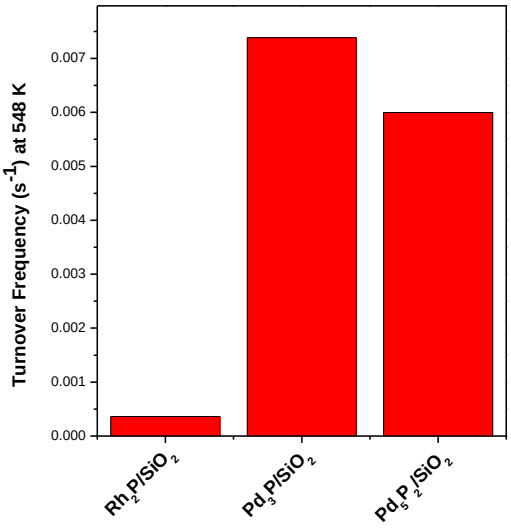


**Figure 4.3 Turnover frequencies (TOFs) for rhodium phosphide and palladium phosphide.**

*Supported ruthenium phosphides ($RuP/SiO_2$ and $Ru_2P/SiO_2$)*

Phase pure silica-supported RuP and $Ru_2P$ catalysts were prepared by TPR in hydrogen of uncalcined $RuCl_3/SiO_2$ precursors impregnated with ammonium hypophosphite. XRD patterns of the $Ru_xP_y/SiO_2$ catalysts prepared in this manner confirm that by varying the phosphorus to ruthenium molar ratio (P/Ru) in the catalyst precursor, different ruthenium phosphide phases were obtained. Using the Scherrer equation, average crystallite sizes were calculated to be 8 nm for the $Ru_2P/SiO_2$ catalyst having P/Ru=0.86 and 10 nm for the $RuP/SiO_2$ catalyst (P/Ru=1.1). TEM images of the $Ru_2P/SiO_2$ and $RuP/SiO_2$ catalysts revealed well-dispersed particles and average particle sizes of 4.1 ± 1.9 nm. The discrepancy in particle sizes determined by XRD relative to those from TEM are

likely due to the fact that the smallest $Ru_xP_y$ particles (< 5 nm) are below the detection limit for XRD and therefore contribute only to the average TEM particle size.

In order to make an assessment of the potential for using Ru phosphide as catalysts to upgrade bio-oils, furan HDO activity measurements were carried out for a series of $Ru_2P/SiO_2$ and $RuP/SiO_2$ catalysts, as well as for a commercial $Co\text{-}Mo/Al_2O_3$ catalyst. As shown in Figure 3.33, all the catalysts exhibited declining furan HDO activity over time; however, the $Ru_2P/SiO_2$ catalyst showed a slower decline in activity after 10 h on-stream than the other catalysts. The $Ru_2P/SiO_2$ catalyst was also significantly more active than the $RuP/SiO_2$ and $Ru/SiO_2$ catalysts, as well as the commercial $Co\text{-}Mo/Al_2O_3$ catalyst; it was almost three times as active as the $RuP/SiO_2$ and $Ru/SiO_2$ catalysts, and over one order of magnitude more active than the commercial $Co\text{-}Mo/Al_2O_3$ catalyst. Interestingly, the $Ru/SiO_2$ and $RuP/SiO_2$ catalysts exhibited very similar furan HDO activities, with the activity of the $RuP/SiO_2$ catalyst dropping just below that of the $Ru/SiO_2$ catalyst near the end of the 38 h testing period.

The furan HDO product selectivities after 24 h on-stream were calculated in order to gain insight into the favored HDO reaction pathway of each catalyst. The product selectivities were found to differ significantly between the Ru phosphide and the Ru metal catalysts, with the $Ru_2P/SiO_2$ and $RuP/SiO_2$ catalysts strongly favoring $C_4$ products and the $Ru/SiO_2$ strongly favored $C_3$ hydrocarbon products. Interestingly, no tetrahydrofuran ($C_4H_8O$) or butadiene ($C_4H_6$) products were observed for any of the catalysts tested. Shown in Figure 4.4, Furimsky[6] has proposed a possible pathway for the hydrodeoxygenation of

furan to account for these observed products, which utilizes a common open-ring intermediate.

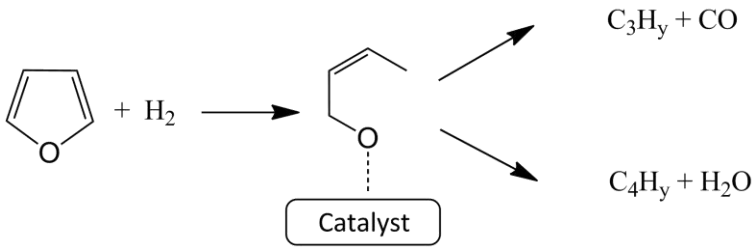


**Figure 4.4 HDO Reaction pathways for furan.[6]**

The $C_4$ hydrocarbons are produced by hydrogenolysis of the remaining C—O bond of the open-ring intermediate, while the $C_3$ hydrocarbons are produced by cleavage of the C—C bond adjacent to the O, resulting in a $C_3$ product and carbon monoxide. Resasco and co-workers[7] recently observed that the preference to favor a particular HDO pathway by a $Pd/SiO_2$ catalyst could be greatly affected by the addition of Cu to form Cu-$Pd/SiO_2$ alloy catalysts. It is possible that the incorporation of P into $Ru/SiO_2$ to from $RuP/SiO_2$ and $Ru_2P/SiO_2$ had a similar effect on pathway preference and, therefore, product selectivity. This hypothesis seems reasonable as a similar effect on product selectivity by P incorporation was observed in the DBT HDS results for the $Rh_2P/SiO_2$ and $Rh/SiO_2$ catalysts performed earlier in this research. Additionally, the production of carbon monoxide may also explain the lower HDO activity of the Ru metal catalysts, as CO has been shown by Badawi et al.[8] to be a major HDO inhibitor, with the CO competing with unreacted organo-oxygen molecules for catalyst active sites. While varying the P/Ru molar ratio during catalyst synthesis was found to affect furan HDO activity of $Ru_xP_y/SiO_2$ catalysts, it did not strongly influence product selectivities. The $Ru_2P/SiO_2$ and $RuP/SiO_2$ catalysts exhibited

excellent phase stability during furan HDO, as the post-HDO XRD patterns reveal no change in phase purity or average crystallite size when compared to the as-prepared catalysts.

The three-fold increase in furan HDO activity after 48 h on-stream by the $Ru_2P/SiO_2$ catalyst in comparison to the $RuP/SiO_2$ and $Ru/SiO_2$ catalysts of similar metal loadings suggest a strong potential for $Ru_2P/SiO_2$ catalysts in the HDO processing of Bio-oils. The $Ru_2P/SiO_2$ catalyst also exhibited superior stability, maintaining nearly steady activity over time, whereas the furan HDO activity by the $RuP/SiO_2$, $Ru/SiO_2$, and commercial $Co-Mo/Al_2O_3$ catalysts continued to decrease over time. In addition to the higher HDO activity, the preference to selectively remove the oxygen without a net carbon loss reinforces the potential of $Ru_2P/SiO_2$ catalysts for upgrading bio-oils.

**References:**

1. Hayes, J. R.; Bowker, R. H.; Gaudette, A. F.; Smith, M. C.; Moak, C. E.; Nam, C. Y.; Pratum, T. K.; Bussell, M. E., Hydrodesulfurization properties of rhodium phosphide Comparison with rhodium metal and sulfide catalysts. *J. Catal.* **2010,** *276* (2), 249-258.

2. Burns, A. W.; Gaudette, A. F.; Bussell, M. E., Hydrodesulfurization properties of cobalt-nickel phosphide catalysts: Ni-rich materials are highly active. *J. Catal.* **2008,** *260* (2), 262-269.

3. Oyama, S. T.; Gott, T.; Zhao, H. Y.; Lee, Y. K., Transition metal phosphide hydroprocessing catalysts: A review. *Catal. Today* **2009,** *143* (1-2), 94-107.

4. Ishihara, A.; Dumeignil, F.; Lee, J.; Mitsuhashi, K.; Qian, E. W.; Kabe, T., Hydrodesulfurization of sulfur-containing polyaromatic compounds in light gas oil using noble metal catalysts. *Appl. Catal. A-Gen.* **2005,** *289* (2), 163-173.

5. Bej, S. K.; Maity, S. K.; Turaga, U. T., Search for an efficient 4,6-DMDBT hydrodesulfurization catalyst: A review of recent studies. *Energ. Fuel* **2004,** *18* (5), 1227-1237.

6. Furimsky, E., The Mechanism of Catalytic Hydrodeoxygenation of Furan. *Appl. Catal.* **1983,** *6* (2), 159-164.

7. Resasco, D. E.; Sitthisa, S.; Pham, T.; Prasomsri, T.; Sooknoi, T.; Mallinson, R. G., Conversion of furfural and 2-methylpentanal on Pd/SiO(2) and Pd-Cu/SiO(2) catalysts. *J. Catal.* **2011,** *280* (1), 17-27.

8. Paul, J. F.; Badawi, M.; Cristol, S.; Payen, E., Guaiacol derivatives and inhibiting species adsorption over MoS(2) and CoMoS catalysts under HDO conditions: A DFT study. *Catal. Commun.* **2011,** *12* (10), 901-905.